UNIVERSITY OF CALIFORNIA

Santa Barbara

QUATERNARY CHRONOLOGY AND UPLIFT OF GAVIOTA COAST MARINE

TERRACES, SANTA BARBARA COUNTY, CA

A Thesis submitted in partial satisfaction of the

requirements for the degree Master of Science

in Earth Science

by

Daniel Lawrence Morel

Committee in charge:

Professor Edward A. Keller, Chair

Professor Kristin Morell

Professor Oliver A. Chadwick

September 2018

The thesis of Daniel Lawrence Morel is approved.

_____

Kristin Morell

_____

Oliver A. Chadwick

_____

Edward A. Keller, Committee Chair

July 2018

Quaternary Chronology and Uplift of Gaviota Coast Marine Terraces, Santa Barbara

County, CA

ACKNOWLEDGEMENTS

ABSTRACT

Quaternary Chronology and Uplift of Gaviota Coast Marine Terraces, Santa Barbara

County, CA

by

Daniel Lawrence Morel

The ~60 km Gaviota Coast of the Western Transverse Ranges, southern California, is a tectonically active region with emergent marine terraces. Rock uplift rates have been questioned near Gaviota Canyon, where the South Branch of the Santa Ynez fault (SBSYF) strikes offshore, oblique to the east-west trending coastline. No absolute dates have been reported within 35 km east of the fault, and unconventional ages reported west of the fault have not been verified. Establishing an accurate terrace chronology is crucial because large (~40 m) differences in paleo-sea level between marine isotope stages (MIS) 3 and 5 significantly change uplift rate estimates, which can impact tectonic models and assessments of seismic hazard. I provide new chronologic constraints for the Gaviota Coast, yielding rock uplift rates up to five times higher than those previously reported west of the SBSYF.

Twelve radiocarbon ages (40-50 ka) and eight optical ages (31-47 ka) from raised beach deposits indicate the first emergent terrace formed during MIS 3. These ages yield time-averaged rock uplift rates between 0.9-2.0 m/ky. In general, higher terrace elevations and rates of uplift (~1.5 m/ky) occur on the eastern Gaviota Coast, though local deviations occur and are controlled by small structures. West of the SBSYF, there is a 16 m drop in the elevation of the first emergent terrace, and rock uplift rates decrease to ~1.1 m/ky. These

rock uplift rates are reaffirmed by the elevation spacing of a flight of five marine terraces preserved on the western Gaviota Coast. The terraces are much younger than previously believed, with the paleo-shorelines correlating to intermediate highstands from MIS 3 to late MIS 5 (45-84 ka), rather than from MIS 5-9. The terrace flight is offset by the SBSYF, with up to 0.44 m/ky of differential uplift accommodated across the SBSYF based on offset of the same-age terrace. A knickpoint in the longitudinal profile of Gaviota Creek, as well as a transition from alluvial to bedrock channel conditions across the fault, indicate the SBSYF is active and has a south-side up component of slip.

These results indicate that relatively high rock uplift rates persist for 110 km from Point Conception to Ventura, where even higher rates (up to 6-7 m/ky) have been reported. Because rock uplift rates on the western Gaviota Coast are higher than previously believed, seismic hazard models for the area should be re-evaluated, as recurrence intervals may be shorter and there may be potential for long ruptures along regional faults (i.e. Pitas Point fault system).

TABLE OF CONTENTS

LIST OF FIGURES AND TABLES

Figures

Tables

INTRODUCTION

Marine terraces and changes in mountain topography record important information about active tectonic processes, including rock uplift rates (e.g. Bull and Cooper, 1986; Burbank et al., 1999; Kirby et al., 2007). The Gaviota Coast, located west of Santa Barbara on southern California's transpressional continental margin (Figure 1), provides an ideal natural laboratory for tectonic geomorphology research because marine terraces are preserved for over ~60 km and parallel the Santa Ynez Mountains. Although these terraces have been studied and dated to estimate rock uplift rates, early work focused on relative dating techniques, such as amino acid racemization and oxygen isotopes (Kennedy et al., 1992; Rockwell et al., 1992; Metcalf, 1994; Trecker et al., 1998). Absolute dates along the Gaviota Coast are sparse, and there is disagreement between older ~80 ka ages near Point Conception (Rockwell et al., 1992) and more recent ~48 ka ages near Isla Vista (Figure 2) (Gurrola et al., 2014). Establishing an accurate terrace chronology is crucial because large (~40 m) differences in paleo-sea level between marine isotope stages (MIS) 3 and 5 significantly change rock uplift rate estimates, which can impact tectonic models and assessments of seismic hazard.

A particular area of interest is near Gaviota Canyon, where the South Branch of the Santa Ynez fault (SBSYF) strikes southwest offshore and intersects with the east-west trending coastline (Figure 2). Geomorphic changes in the Santa Ynez Mountains, including an abrupt 350 m decrease in average mountain crest elevation from east to west across the SBSYF (Tierney, 2002; Wampler, 2013), suggest the fault may form a structural boundary between two tectonic segments of the Gaviota Coast.

This study seeks to understand along-strike variability in rock uplift rates on the Gaviota Coast by constraining the chronology of the first emergent terrace. The previously reported MIS 3 terrace age to the east yielded high rock uplift rates (~1.6 m/ky), while the MIS 5 age to the west yielded low rock uplift rates (0.15-0.3 m/ky). These conflicting results point toward two probable scenarios: (1) a gradual decrease in rock uplift rates over 40 km from east to west; or (2) an abrupt step-wise decrease in rock uplift rates across the SBSYF, which juxtaposes terraces of different ages. To test these hypotheses, I present a geochronologic dataset from the first emergent terrace spanning ~55 km between Cojo Bay and Isla Vista. Age control was obtained using radiocarbon dating on marine mollusk shells and optically stimulated luminescence (OSL) on raised beach sands. Terrace elevations were determined using airborne LiDAR and field measurements. With these data, I estimate time-averaged rock uplift rates and discuss them in the context of the regional tectonic framework. To test for differential uplift across the SBSYF, I present a longitudinal stream profile of Gaviota Creek and field observations of the channel where it crosses the fault. Finally, I evaluate the possibility of Holocene terraces along the Gaviota Coast, and address this study's implications for future assessments of seismic hazard.

BACKGROUND

Tectonic and geologic setting

The Gaviota Coast, defined as the ~60 km long east-west trending shoreline between Point Conception and Isla Vista, lies within the Western Transverse Ranges physiographic

province of Southern California (Figure 1). The Western Transverse Ranges are experiencing active uplift and north-south crustal shortening (Larson and H., 1992; Marshall et al., 2013) associated with the restraining bend ("the Big Bend") in the San Andreas fault (SCEC, 1995). Paleomagnetic data also indicate that this region has undergone ~90˚ clockwise crustal block rotation since 15 Ma (Hornafius et al., 1986; Luyendyk, 1991). Locally, shortening is accommodated by the growth of the Santa Ynez Mountains and the Santa Barbara Fold Belt, an east-west trending belt of folds and faults on the south flank of the Santa Ynez Range and offshore in the Santa Barbara Channel (Keller et al., 2007) (Figure 2).

The Gaviota Coast is bound to the north by the Santa Ynez Mountains and the Santa Ynez fault, a steeply south-dipping left-reverse fault that follows the northern flank of the range and extends for at least 130 km (Jennings, 1994) (Figure 2). Although exposures of the fault are rare and often buried by material shed from the adjacent mountain slope, significant offsets on the order of several km have been deduced from juxtaposed rocks of Upper Cretaceous to Miocene age (e.g. Dibblee, 1966; Table 1 in Sylvester and Darrow, 1979). Recent fault activity is suggested by left-lateral deflections of active stream channels draining the north slopes of the Santa Ynez Mountains. The longest of these is Escondido Creek at Blue Canyon, which follows the fault for 3 miles before resuming its northern course to the Santa Ynez River (Dibblee, 1966).

The Santa Ynez fault bifurcates near Gaviota Canyon, with the north branch continuing west through the axis of the range (Sylvester and Darrow, 1979) and the south branch (SBSYF) turning southwest and striking offshore (Figure 2). The SBSYF is unique among regional structures because it obliquely cuts across the east-west structural grain of

the Santa Ynez Mountains and Santa Barbara Fold Belt (Johnson et al., 2017). Reported dips on the SBSYF vary from 60-80 degrees N to NW (Dibblee, 1950; Yerkes et al, 1981; Wampler, 2013), possibly a consequence of the complex 4 m-wide shear zone exposed in the sea cliff where the fault strikes offshore. Trenches excavated across the SBSYF on the coastal plain have indicated south-side up displacement of Late Pleistocene terrace deposits, but no certain Holocene activity (Dibblee, 1978; Sylvester and Darrow, 1979; Yerkes et al., 1981). Alternate senses of slip have been proposed (i.e. Johnson et al., 2017), and there is also potentially a component of left-lateral slip based on fold axes offshore that are offset by as much as 820 m (Yerkes et al., 1981), and apparent offsets in stream drainages both on and offshore (Eichhubl et al., 2002). No seismicity has been recorded on the fault (Southern California Earthquake Data Center, 2018).

Numerous faults have been mapped offshore in the Santa Barbara Channel using seafloor bathymetry and seismic reflection profiles (Sorlien and Nicholson, 2015; Johnson et al., 2017). The most significant of these is the Pitas Point fault (Figure 2), a blind, north-dipping reverse fault that continues all the way from Point Conception to Ventura (Johnson et al., 2017), where it is referred to as the Ventura fault onshore.

The regional bedrock geology consists of Cenozoic sedimentary rocks deposited in a continental margin setting. Geologic maps and cross sections (Dibblee, 1966; Redin et al., 2005) suggest the Santa Ynez Mountains are a large, south-dipping homoclinal (to variably anticlinal) structure on the hanging wall of the north-dipping Pitas Point fault. Bedrock is well-exposed in the mountains, and lithologic contacts strike nearly parallel to the mountain range crest. Quaternary alluvial fan deposits sourced from the mountains cover the coastal plain, forming a single broad, gently-sloping piedmont surface.

Near Santa Barbara, coastal deformation is apparent in the landscape as a series of mesas (i.e. Mission Ridge) and troughs, which are surficial expressions of folds and blind oblique-reverse faults in the Santa Barbara Fold Belt (Gurrola et al., 2014). On the Gaviota Coast between Point Conception and Refugio Canyon, there are no such obvious topographic expressions of deformation on the coastal plain. No major faults have been mapped besides the SBSYF (Figure 2). Yet, emergent marine terraces serve as evidence of an actively uplifting coastline.

Marine terraces

Marine terraces have been studied as early as the 1890s, when Lawson (1893) described five distinct platforms near Santa Cruz, California. Terraces initially form at sea level, where wave action, sediment abrasion, and tidal flux bevel bedrock into a flat surface, the modern wave-cut platform. As tectonic uplift occurs and/or sea level falls, marine sands and/or alluvium and colluvium are deposited atop this bedrock surface (Bradley, 1957), which is known as the paleo-wave-cut platform or paleo-marine abrasion surface (Figure 3). When a wave-cut platform is raised above sea level, it is preserved as a marine terrace.

It is thought that terrace platforms are cut during eustatic highstands (Bradley and Griggs, 1976), due to the clustering of radiometric ages on erosive terraces during times of high sea level (e.g. Bradley and Addicott, 1968; Ku and Kern, 1974). This hypothesis has been further supported by work on constructive carbonate terraces dated to the same eustatic highstands in Barbados, the Indian Ocean, and the Pacific Ocean (e.g. Broecker et al., 1968; Chappell, 1974; Bloom et al., 1974).

Marine terraces are frequently studied by geomorphologists because they have a characteristic geometry (Figure 4) that provides insights to a coastline's tectonic history. If

the age of a marine terrace can be determined, its present elevation measured, and the position of paleo-sea level is known at the time of platform beveling, a time-averaged rate of rock uplift can be calculated (Lajoie et al., 1979). The landward edge of an uplifted marine terrace, or paleo-shoreline angle, is defined by the intersection of the paleo-sea cliff with the paleo-marine abrasion surface; this paleo-shoreline is presumed to approximate the level of high tide at the highstand when the terrace platform was cut (Bradley, 1957). Thus, a flight of marine terraces and the associated paleo-shoreline angles provide a record of past sea levels (Gurrola et al., 2014). Higher terraces reflect older marine platforms that have experienced more uplift. If a constant rate of uplift is assumed, an entire flight of successive terraces can be dated given the age of only one terrace, the other terrace elevations, and a sea level curve (Bradley and Griggs, 1976; Bull, 1985).

Previous work

Gaviota terrace chronology

Though marine terraces in the Santa Barbara region have been studied, key questions about the Gaviota Coast's tectonic history and rate of uplift remain unresolved. Historically, absolute dating of terraces along the Gaviota Coast was precluded by a scarcity of fossil corals for Uranium-series (U-series) dating, and the limits of mass spectrometry on radiocarbon dating. Thus far, only two studies have reported absolute terrace ages:

Rockwell et al. (1992) mapped and dated terraces west of Gaviota Canyon. Trench logs and borehole data for a proposed natural gas facility (Dames and Moore, 1980) provided a lens through the alluvial cover, permitting mapping of the bedrock surface and shoreline angles of five marine terraces. The first emergent terrace was assigned an age of

80 ka (MIS 5) based on U-series dates on mammal bones sampled from terrace deposits (Rockwell et al., 1992). This 80 ka age yielded low uplift rates between 0.15-0.3 m/ky. The lack of further chronologic constraints at the time prompted researchers to project the 80 ka age eastward across the SBSYF, based on results from relative dating methods (Rockwell et al., 1992; Muhs et al., 1992; Metcalf, 1994). Consequently, these studies proposed low rock uplift rates for the Gaviota Coast (0.15-0.3 m/ky), which are still regularly cited today.

Further east at Ellwood Mesa and Isla Vista (Figure 2), Gurrola et al. (2014) used several methods, including U-series on coral and optically stimulated luminescence, to assign a terrace age of 48 ka (MIS 3) and a higher rock uplift rate of 1.6-1.8 m/ky. These results contradicted the 80 ka age and low uplift rates from the western Gaviota Coast, providing the motivation for this study.

Geomorphology of the Santa Ynez Mountains

Research has shown that geomorphic indices including elevation, relief, and stream channel gradients normalized for upstream drainage area (k_{sn}), are sensitive to changes in rock uplift rate (e.g. Kirby and Whipple, 2001; Wobus et al., 2006; Morell et al., 2015). Thus, remote analysis of the Santa Ynez Mountains through digital elevation models (DEMs) has provided key insights about spatial trends in rock uplift.

For example, recent quantitative geomorphologic analysis has suggested that rock uplift rates may change across the SBSYF. Mean k_{sn} indices of stream channels to the east (29.4) are nearly double those to the west of the fault (17.3) (Duvall et al., 2004; Wampler, 2013), yet lithology and climate remain consistent along the Santa Ynez Mountain front. Furthermore, the mean mountain-crest elevation and topographic relief of the range abruptly increase across the fault from west to east (Figure 5), and the Santa Ynez Mountains can be

split into distinct geomorphic segments based on these characteristics (Tierney, 2002; Keller and DeVecchio, 2013). These data suggest that the SBSYF separates two tectonic segments of the Gaviota Coast, and that the eastern portion is uplifting more rapidly. To test this hypothesis, I use radiocarbon and optical dating to resolve the terrace chronology and quantify rock uplift rates across the SBSYF.

METHODS

Over 55 km of coastline between Cojo Bay and Isla Vista were traversed to find exposures of the first emergent terrace suitable for absolute dating. Accessible exposures with marine mollusk fossils and/or marine sands directly overlying the paleo-marine abrasion surface were selected as sample sites. Age control at each site was established through radiocarbon dating and/or optically stimulated luminescence (OSL).

In order to elucidate along-shore changes in rock uplift, I focused on collecting a geographically extensive geochronologic dataset from the first emergent terrace. Although higher marine terraces have been identified along the Gaviota Coast (Upson, 1951; Rockwell et al., 1992), these relict terraces have been heavily incised and eroded, and are poorly preserved and laterally discontinuous. Datable exposures of older terraces are scarce because they are often buried by thick alluvial deposits that blanket the coastal plain (up to 17 m in some sea cliff outcrops). When exposures do occur, typically little material remains from the original terrace deposits, precluding dating. The first emergent terrace, however,

has numerous accessible outcrops exposed in the modern sea cliff that host datable material, and these are the sites I targeted for this study.

Radiocarbon dating

Twelve marine mollusk samples were submitted to the Keck Carbon Cycle Accelerator Mass Spectrometry facility at the University of California Irvine for radiocarbon analysis. Samples were physically cleaned and leached with dilute HCl following standard protocols to remove potential external secondary alteration. In the field, I collected shell samples that had the least potential for reworking when possible, such as endolithic bivalves in growth position or articulated bivalves. Thin-walled but intact disarticulated bivalves or gastropods were collected when such samples could not be found.

Optically stimulated luminescence dating

Terraces west of the SBSYF were expected to exceed the upper limits of radiocarbon dating (~50 ka without isotopic enrichment; Walker, 2005), so optically stimulated luminescence (OSL) was also pursued because its range extends to over 200 ka. OSL provides a means to determine the burial age of sediments directly (typically fine sand to silt-sized grains). Optical dating works on the principle that naturally-occurring radioactive isotopes (^{40}K, ^{232}Th, ^{238}U, ^{87}Rb) in sediments undergo decay and subject adjacent material to low-levels of radiation (Huntley et al., 1985). This ionizing radiation frees electrons in adjacent quartz and feldspar grains from their normal atomic sites, and some of these freed electrons become trapped at structural defects or holes within the crystal lattice that have a net positive charge (For example, where aluminum substitutes for silica in quartz, which produces an electron hole center; Weil, 1984). The longer a sample is buried, the longer it is

9

exposed to ambient radiation, and the greater the intensity of the luminescence signal that is later measured in the lab (Rittenour, 2008). The radiation dose emitted in a given environment each year, or dose rate, can be determined by measuring the concentration of radioactive isotopes in sediments adjacent to a sample (Guérin et al., 2011).

Crucially, when a sample is exposed to sunlight, its electron traps are emptied by the stimulation of photons, which "zeroes" the sample's energy signal or luminescence clock (Aitken, 1998). This process is known as bleaching. Sample luminescence is finally measured in the lab, and the iterative SAR protocol (Murray and Wintle, 2000) is used to determine the corresponding level of radiation stored in a sample, or the equivalent dose. Thus, an OSL age can be determined by dividing the equivalent dose by the background dose rate.

OSL is an ideal geochronometer for this study because the method spans the appropriate timescale, and its resolution (typically 1σ uncertainty $\pm$ 5-10%; Rhodes, 2011) is sufficient to distinguish between the expected ages of MIS 3 and 5. Moreover, nearby terraces have been successfully dated with OSL (Gurrola et al., 2014). I targeted raised beach sands, which have optimal characteristics for OSL analysis: fine-medium sand grain size, well-sorted and homogeneous material (which minimizes dose rate errors), and a depositional environment that involves significant transport before burial. Thus, quartz grains are likely to be well-bleached and have a uniform luminescence signal (Madsen and Murray, 2009; Rhodes, 2011).

I collected OSL samples at seven sites where raised beach sands overlie the paleo-marine abrasion surface, following sampling protocols outlined by Nelson et al. (2015). To check the methodology, a replicate pair was collected at one site. Samples were shielded

from sunlight by driving a stainless steel pipe (20.32x3.81 cm) into a freshly cleaned

outcrop. To minimize possible post-deposition mixing, I targeted sands with intact

sedimentary structures (Duller, 2008). I then collected sediment within a ~30 cm radius of

the sample tube for the environmental dose rate. OSL samples were collected as close to the

paleo-marine abrasion surface as possible, while remaining at least 30 cm away from the

bedrock contact and any nearby gravel horizons to avoid dose rate complications. Samples

were processed and analyzed at Utah State University's Luminescence Lab (for detailed lab

procedures, see appendix).

Elevation data and analysis

Terrace elevations were determined using a 0.5 m coastal LiDAR dataset (last-return

vertical accuracy ±11.6 cm; DOC/NOAA/NOS/OCM, 2016) and field measurements. Site

locations were acquired with GPS, and sample elevations were determined using the LiDAR

dataset and field measurements. For any spatial analysis over ~0.5 km inland, including a

relief map of the Santa Ynez Mountains and a longitudinal profile of Gaviota Creek, a 3 m

IfSAR DEM was used (DOC/NOAA/NOS/ OCM, 2004). This longitudinal profile was

generated using TopoToolbox2 Matlab codes (Schwanghart and Scherler, 2014).

Paleo-sea level elevations

To estimate rock uplift rates, the total vertical displacement of an elevated terrace

must be calculated by subtracting the modern terrace elevation from paleo-sea level at the

time of platform beveling. This procedure can have a substantial impact on rock uplift rates

because Pleistocene glacial cycles have induced drastic fluctuations in eustatic sea level

(Shackleton, 1987). Although eustatic sea levels are relatively well constrained for the late

Pleistocene (Lambeck and Chappell, 2001), this curve is not appropriate for the Santa Barbara area because local sea levels can be markedly different due to the effects of glacial isostatic adjustment (GIA), which vary in magnitude by latitude. Thus, selecting an appropriate sea level curve for a given study area is crucial.

For this study, I use a local sea level curve by Simms et al. (2016), which accounts for the effects of GIA. This curve was selected over other available models (e.g. Muhs et al., 2012) for several reasons: 1) it was calibrated for the latitude of Gaviota, CA, making it the nearest paleo-sea level curve available; 2) the curve captures smaller-scale fluctuations in sea level that are not present in other models; 3) the curve was calibrated using marine terraces along the entire Pacific Coast, providing sufficient control to test the model; and 4) multiple Earth mantle rheology parameters were objectively considered in the curve's development. Simms et al. (2016) selected the Earth mantle model that produced a sea level curve with the best fit compared to a longitudinal transect of paleo-sea levels derived from terraces along the Pacific Coast.

Rock uplift rate calculations

Time-averaged rock uplift rates (U) were estimated using the following equation:

$$U = (E - pSL) \, / \, T$$

where E is the modern terrace elevation, T is the sample age, and pSL is the paleo-sea level elevation at time T. Uncertainties in rock uplift rates (ε_U) were calculated propagating errors, following the form:

$$\varepsilon_U = U * \sqrt{[(\varepsilon_T/T)^2 + (\varepsilon_{Vd}/V_d)^2]}$$

where ε_T is the uncertainty in the sample age, and ε_{Vd} is the compounded uncertainty in vertical tectonic displacement from all elevation measurements, according to:

$$\varepsilon_{Vd} = \sqrt{[\varepsilon_{pSL}{}^2 + \varepsilon_{Li}{}^2 + \varepsilon_{FM}{}^2]}$$

where ε_{pSL} is the uncertainty in the paleo-sea level, ε_{Li} is the uncertainty in the LiDAR data set, and ε_{FM} is the uncertainty in field measurements.

Ideally, rock uplift rates are derived using a terrace's paleo-shoreline angle elevation, which approximates the mean paleo-sea level highstand (Bradley, 1957). However, the landward edges of marine platforms along the Gaviota Coast are buried under thick alluvial cover. Paleo-shoreline elevations can be estimated by projecting the platform surface up-gradient from sea cliff exposures to its intersection with the paleo-sea cliff, but paleo-sea cliffs east of Gaviota Canyon are not clearly discernible; the coastal plain here is relatively narrow, and construction of Highway 101 has obscured these geomorphic features. Even where the coastal plain is wider by Naples Point, topographic profiles drawn perpendicular to the shoreline did not reveal any clear scarps indicating paleo-sea cliffs or higher terraces. Thus, rather than make uncertain inferences about paleo-shoreline angle elevations, I report uplift rates using the sample elevation exposed in the modern sea cliff, which is readily observed in the field and can be reported objectively.

RESULTS

Pleistocene marine terrace deposits

The first emergent terrace is well-preserved and nearly laterally continuous from Point Conception to Isla Vista, apart from areas where it has been eroded at sloughs or stream drainages, and a 5 km stretch west of the SBSYF. The terrace varies in width from

~500 m (Cojo Bay) to <50 m (just west of Gaviota Canyon). In general, the coastal plain is narrower along the central Gaviota Coast, and widest to the west between Point Conception and Arroyo Bulito, and to the east between El Capitan State Park and Isla Vista.

Uplifted terraces can be readily identified in the modern sea cliff by an abrupt truncation of the (generally) south-dipping bedrock (Figure 3). This beveled, planar bedrock contact reflects the paleo-wave-cut platform, and represents an angular unconformity between the Miocene bedrock (most commonly the siliceous shales of the Monterey and Sisquoc Formations) and overlying Quaternary terrace deposits.

The paleo-marine abrasion surface commonly exhibits evidence of bioturbation in the form of borings from endolithic marine mollusks (i.e. Pholadidae or *Platydon cancellatus*) and burrows (i.e. *Polydora*), confirming that it was once a near-shore marine setting (Figures 6a and 6b). The bedrock contact is commonly overlain by a bed of rounded cobbles (sometimes with a shell-sand matrix), which may also exhibit mollusk borings. This layer is thought to represent the transgressive ravinement surface, a flooding surface that forms when paleo-sea level rises and causes reworking of the shoreline (Catuneanu, 2006). Locally, 1-2 m packages of white, quartz-rich, moderately-well sorted sand with parallel laminations are found overlying the basal cobble bed (Figure 6c, 6d, 6e). Given their sedimentology and stratigraphic context, these sands are interpreted as marine foreshore deposits. Tar blebs, gravel beds, and cobbles with mollusk borings are also occasionally found within the sand units. The foreshore sands were likely deposited during a forced regression as sea level fell following a highstand, resulting in beach progradation.

Weakly to moderately consolidated terrestrial alluvial deposits are ubiquitous and cap the marine terrace sequence above the marine sands (Figure 6d), or directly overlie the

abrasion surface if no marine sands are present (Figure 3). These terrace-cap deposits are quite variable, ranging from massive siltstones, to siltstones and matrix-supported breccias with indistinct bedding, to interbedded silts, coarse sands (occasionally with cross-beds) and clast-supported breccias. All deposits exhibit characteristics typical of alluvial fan deposits, with poor sorting, angular clasts (usually of the Monterey Formation), and paleosol horizons with visible root traces, suggestive of hiatuses in deposition between pulses of debris flow-style deposition. Adjacent to some drainages (i.e. west of Gato Canyon and east of Dos Pueblos Canyon), stratified fluvial conglomerates directly overly the paleo-marine abrasion surface, suggesting that some degree of meandering and fluvial deposition occurred following a drop in base level, before the streams incised to modern sea level.

Marine mollusk shells collected for radiocarbon dating were found in a variety of sedimentological contexts. At ENP (abbreviations refer to site locations in Tables 1 and 4), a shell hash layer directly overlies the paleo-marine abrasion surface (Figure 6a). At WGV and WGV2, shells are mixed in with the basal cobble bed (Figure 6f). The remaining sites (WLV, EBC, IV, COJ) host rich fossil shell assemblages directly overlying the bedrock contact. WLV contains a fossiliferous ~20 cm mud layer with occasional small rounded cobbles and at least one fully articulated bivalve. The Isla Vista site hosts a ~70 cm thick silt-fine sand deposit with abundant well-preserved specimens and few clasts, suggesting a calmer, potentially lagoon setting. The Isla Vista site is also unique in that it hosts endolithic bivalves in life position, bored into the uplifted bedrock marine abrasion surface. Two articulated endolithic *Platydon cancellatus* shells were collected here. The EBC and COJ sites contain several shell beds interbedded with marine sands; at EBC the shell beds are poorly stratified, while at COJ the shells are well-stratified and form distinct horizons.

15

Except for the two eastern sites (EBC and IV), none of these fossil localities have been radiometrically dated prior to this study.

Terrace chronology

Both radiocarbon and OSL samples consistently yielded ages between 31-50 ka (Tables 1 and 4), indicating the first emergent terrace formed during MIS 3 (Figure 7). Calibrated radiocarbon ages (Table 1) range from 39.6-50 ka, with a mean of 45 ka. There is good replication across all twelve samples from seven sites, and samples collected at the same site agree. The median radiocarbon ages of the western-most samples (COJ 1 & 2, 48.1 and 44.9 ka) are similar to those of the eastern-most samples (IV 1 & 2, 49.0 and 47.9 ka), showing no obvious change in chronology over the study area.

Although some studies have raised questions about the reliability of radiocarbon dating on older marine shells (e.g. Price et al., 2011; Busschers et al., 2014), radiocarbon ages from this study closely agree with and are well-supported by optical ages and U-series ages on coral obtained by Gurrola et al. (2014) at two of the same sites (Table 2). Some sample ages (i.e. COJ 1, WLV 3, ENP) may be older than others because shell dating captures time of mollusk death, not time of deposition. Additional scatter between sites could be caused by variations in terrace width.

Eight OSL ages range from 31-47 ka (Table 4). Overall, OSL ages corroborate the radiocarbon ages, and ages from the same site or adjacent sites agree (i.e. WLV_osl and WLV 1-2; ENP_osl and ENP, and EAC_osl and WGV). Most samples exhibit good luminescence properties and are well-bleached, as indicated by the symmetry and lack of long-tails in their equivalent dose distributions (see appendix). Once again, ages are consistent, and there is no evidence of a spatial trend in the sample chronology.

Optical ages reflect a minimum age for the paleo-wave cut platform because raised beach sands targeted for dating were likely deposited during a forced regression as beaches prograded and sea level fell following a eustatic highstand. Thus, these raised beach sands were deposited some time after the bedrock abrasion platform had already been cut. This sequence is supported by the fact that the optical ages tend to be slightly younger than the radiocarbon ages (Figure 7). Additionally, the raised beach sands were stratigraphically higher in sea-cliff outcrops than the dated shell deposits, which were at or just above the paleo-marine abrasion surface. Thus, despite the apparent age offset, the two datasets capture similar terrace ages.

Adjacent OSL sample pairs WSAG_osl1 and WSAG_osl2 are similar, and WNP_osl and ENP_osl1 are within error of one another. However, the replicate sample pair collected at ENP exhibits an age inversion, with the stratigraphically lower sample (ENP_osl1) returning a younger age than the higher sample. Because (1) there is no clear stratigraphic reason for this age inversion, (2) the higher sample (ENP_osl2) agrees with the radiocarbon age collected at the site, and (3) the lower sample exhibited poor luminescence properties (it required the most aliquot runs of any sample to obtain an optical age), the lower, younger sample age (ENP_osl1) is excluded from rock uplift rate calculations.

Pleistocene rock uplift rates

The terrace ages yield relatively high time-averaged rock uplift rates for the Gaviota Coast, ranging from 0.9-2.0 m/ky (Tables 1 and 4). Rock uplift rates derived from radiocarbon ages are between 0.9-1.8 m/ky. Those derived from OSL ages range from 1.3-2.0 m/ky. Uplift rates are highest (~1.5 m/ky) and relatively constant along the central

Gaviota Coast between the SBSYF and Ellwood Mesa (Figure 8). Uplift rates are lowest at

Isla Vista and Cojo Bay (~1.0 m/ky).

In general, the eastern Gaviota Coast is uplifting faster than the western portion

(Figure 8). This is also evidenced by higher terrace elevations to the east; west of the

SBSYF, low terrace elevations (~7-8 m) persist for over 10 km (Figure 9). Notably, the OSL

and radiocarbon ages collected west of the fault do not agree (~32 ka at WSAG vs. ~45 ka at

Cojo Bay). Consequently, the younger OSL ages yield higher rock uplift rates (~1.9 vs. ~1.0

m/ky). However, given the low terrace elevations west of the SBSYF, I consider the OSL-

derived uplift rates to be anomalously high, and maintain that the ~1 m/ky radiocarbon-

derived rock uplift rates are more representative of the western Gaviota Coast.

Longitudinal profile of Gaviota Creek

The change in terrace elevations and spatial distribution of rock uplift rates indicates

there is differential uplift accommodated across the SBSYF. Because fluvial systems are

sensitive to tectonic forcing (e.g. Jackson et al., 1996; Keller et al., 1999; Holbrook and

Schumm, 1999), and empirical laboratory studies have shown that channel gradients

increase downstream of an axis of uplift (Ouchi, 1985), one can examine where Gaviota

Creek crosses the fault in Gaviota Canyon to test for differential uplift.

A longitudinal profile of Gaviota Creek (Figure 10) shows a distinct knickpoint as

the creek crosses the SBSYF. Lithologic control is not responsible for this increase in

gradient because Gaviota Creek passes through similar sandstone units across the fault (Ta

upstream and Tsass downstream; Dibblee, 1988). In addition, the Gaviota Creek channel

bottom exhibits a distinct change in character across the fault. Upstream, there is ponding of

alluvium; the creekbed is blanketed in sand, gravel, and small cobbles, with a muddy bottom

in calmer sections (Figure 10). Downstream of the fault, however, the creek abruptly shifts to a bedrock channel, with smooth chutes cut into the sandstone, and only minor accumulations of alluvium in pools or eddies.

DISCUSSION

Updated geochronology dates the first emergent terrace on the entire Gaviota Coast to MIS 3—there is no changeover to a MIS 5-age terrace across the SBSYF. These findings are significant because the MIS 3 ages yield rock uplift rates over five times higher than previous estimates on the western Gaviota Coast (~1.0-1.5 m/ky vs. 0.15-3 m/ky). This has implications for how rock uplift rates change along strike. Rock uplift rates are higher and relatively constant on the eastern Gaviota Coast, and there is only a slight step-wise decrease in rock uplift rate to the west across the SBSYF. This aligns with east to west decreases in topography, relief, and stream channel steepness (k_{sn}) in the Santa Ynez Mountains across the SBSYF (Tierney, 2002; Wampler, 2013). Modeled north-south crustal shortening rates based on geodetic velocity data are also lower on the western Gaviota Coast (~2.5 mm/yr) compared to the central Santa Barbara channel (~6.5 mm/yr; Marshall et al., 2013).

Beyond this general east-to-west trend, spatial variability in rock uplift rates is more complex. Localized areas of reduced rock uplift still occur, and can be linked to mapped structures. Because the entire first emergent terrace is MIS 3 in age, notable changes in the paleo-marine abrasion surface elevation can be used to help elucidate along-shore changes in rock uplift. An along-shore profile of the abrasion surface elevations (Figure 9) illustrates where structures deform the terrace.

Rock uplift rates are relatively constant (~1.5 m/ky) between the SBSYF and

Ellwood Mesa along the central Gaviota Coast, where terrace elevations are higher and few

faults deform the coastal plain. At Isla Vista, uplift rates are lower (~1.0 m/ky) due to

structural control by a syncline and the Isla Vista fault (mapped by Minor et al., 2009 and

Johnson et al., 2017), which both downwarp the terrace locally. The E-W striking More

Ranch fault also offsets the terrace by ~7 m west of Isla Vista, where the fault intersects the

coastline. Low terrace elevations at Isla Vista continue east for less than 5 km, as the More

Ranch fault uplifts the landward side of the first emergent terrace east of Goleta Beach.

Further east, terrace elevations rise to over 30 m at More Mesa.

In contrast, on the western Gaviota Coast, low terrace elevations (~7-8 m) persist for

over 10 km. The radiocarbon ages from Cojo Bay yield a rock uplift rate of 0.9-1.0 m/ky,

but a dip in terrace elevation indicates the site is locally downwarped by the Government

Point syncline (Figure 9). Given the terrace age (~45 ka) and slightly higher and consistent

terrace elevations to either side, a rock uplift rate of 1.1 m/ky is more representative for the

coastline between SBSYF and Point Conception.

Chronology refinement and relict terrace correlation

Rockwell et al. (1992) originally assigned a terrace age of 80 ka to the first emergent

terrace. Four higher terraces were also mapped on the western Gaviota Coast, and these

relict terraces were correlated to major highstands in eustatic sea level at MIS 5c, 5e, 7, and

9—as old as ~340 ka. However, this terrace chronology was based on limited age control at

the time from U-series dates on mammal bones, which are not associated with a marine

setting. These bones may have been recycled and thus may not reflect the true age of the

deposit overlying the paleo-wave cut platform. Furthermore, bone is an unconventional

material for U-series dating because it is not a closed system; migration of U in and out of a sample during its burial history can lead to problematic results (Kennedy et al., 1992; Schwarcz, 1997). Using modern techniques, this study dates the first emergent terrace to MIS 3, which consequently dictates younger ages for the four higher terraces as well. In light of the newly acquired radiocarbon and OSL ages, the previously reported terrace ages must be reconsidered.

To test the rock uplift rates from this study and to refine the chronology of the higher, older terraces, I use the elevation spacing of the flight of terraces mapped by Rockwell et al. (1992) (Figure 11). Following Bull (1985), a constant rate of uplift is assumed, and the terrace shoreline elevations and sea level curve are used to assign ages to the higher terraces. Because there is differential uplift across the SBSYF and the fault offsets this flight of terraces, two rock uplift rates (1.5 m/ky and 1.1 m/ky) are projected from two sets of shoreline angle elevations on either side of the fault.

Despite starting from different elevations, projected uplift rate paths for same-age terraces converge on the same local sea level highstands. Rather than being associated with major highstands (MIS 5, 7, 9), this correlation indicates that these terraces formed during younger, smaller highstands of MIS 5a (84 ka), MIS 4 (71 ka), and MIS 3. Most striking of all, the data show that multiple terraces were cut within MIS 3 at 60, 49.5, and 45 ka.

The terrace correlation also has implications for modeling of paleo-sea level. For example, for the lowest terrace, the two projected uplift rate paths intersect at 45 ka, but just above the highstand on the sea level curve (Figure 11). This could imply that model predictions of GIA effects on sea level for the Santa Barbara region are slightly underestimated at the 45 ka highstand. For the MIS 5a terrace, the two projected uplift rate

21

paths converge from markedly different modern terrace elevations, but they undershoot the 84 ka highstand (estimated to be -4 m locally) by 12 and 16 m. This suggests that this portion of the paleo-sea level curve is poorly constrained, which makes sense because the local MIS 5a sea level was initially calibrated using the previously reported 80 ka Gaviota terrace age (Simms et al., 2016). With the updated chronology indicating an age of MIS 3, the Gaviota terrace should not be used as a reference point for the MIS 5a highstand. Instead, the terrace correlation indicates the MIS 5a local sea level may have been as low as -20 m below sea level (for reference, eustatic sea level was -26 m at 84 ka; Lambeck and Chappell, 2001). Notably, the two projected uplift paths do not exactly intersect at the expected MIS 5a highstand (Figure 11). This could suggest that rock uplift rates changed between 70-84 ka, but this turn out to hold little weight, as only a slight change in the assumed rock uplift rates (<0.05 m/ky) is needed to re-align the two projected uplift rate paths at 84 ka.

The radiocarbon and OSL ages reported in this study suggest the first emergent terrace could have been cut during the highstands at 49.5 ka, 45 ka, or 37 ka on the local paleo-sea level curve. However, given the calculated rock uplift rates, the 37 ka highstand is too young to produce the observed terrace elevations along the Gaviota Coast. There may have been a lower 37 ka terrace at one point, but if so it has been removed by sea cliff retreat. Considering the uplift history and elevation spacing of relict terraces allows for further age constraints on the first emergent terrace: the terrace correlation (Figure 11) indicates an age of 45 ka near the SBSYF. Because the first emergent terrace is laterally continuous and no other major structures crosscut the coastline, it is presumed to be 45 ka along most of the Gaviota Coast.

At Isla Vista, however, which has the lowest terrace elevations and rock uplift rates on the eastern Gaviota Coast, it is possible that first emergent terrace formed during the 49.5 ka highstand. The two radiocarbon samples collected here (mean age of 48.5 ka) were mollusks in life position bored into the marine abrasion surface, and so cannot be older than the time when emergence occurred and beveling of the platform ceased. Thus, these radiocarbon ages likely reflect the time of active platform cutting, suggesting an age of 49.5 ka for the Isla Vista terrace (within analytical error of both samples). Unfortunately, paleo-shorelines of older terraces are not preserved here, so this cannot be checked against uplift histories like on the western Gaviota Coast.

Uncertainty in uplift rates

Rock uplift rates were calculated using sample elevations, though paleo-shoreline angle elevations are typically used (see Methods). As a form of sensitivity analysis, rock uplift rates were recalculated at three sites (four samples) for which paleo-sea cliff scarps are preserved and paleo-shoreline elevations were available from previous work (Rockwell et al., 1992). Results from this analysis yielded minor differences: terrace elevations increased by only 0.4 to 7 m, and rock uplift rates increased by 0-0.2 m/ky. The successful terrace correlation lends further confidence to the reported rock uplift rates, demonstrating they are representative for the Gaviota Coast.

Although the reported terrace ages at Isla Vista (~48 ka) are nearly identical to those of Gurrola et al. (2014), our uplift rate estimates diverge (~1.0 m/ky vs. 1.6 m/ky). This deviation occurs because I use a newer, more refined sea level curve (Simms et al., 2016). This curve reports MIS 3 paleo-sea level to be ~20 m higher than the curve used by Gurrola et al. (2014), resulting in a lower vertical terrace displacement, and thus a lower uplift rate. This

comparison underscores the importance of paleo-sea level in uplift rate calculations, which is usually the greatest source of uncertainty if reliable terrace chronology can be obtained.

Differential uplift on the Gaviota Coast

The SBSYF appears to play a key role in the tectonic geomorphology of the Gaviota Coast, as rock uplift rates and terrace elevations change across the fault (Figure 9). The rate of differential uplift can be calculated by measuring the vertical offset of a surface of known age—in this case, a marine terrace. However, care must be taken when correlating terraces across considerable faults, as displacement may have juxtaposed terraces of different ages. This highlights an important question: is the first emergent terrace on either side of the SBSYF truly the same age?

East of the fault, radiocarbon and OSL ages confirm the first emergent terrace is 45 ka. West of the fault it has also been constrained to 45 ka at WSAG and Cojo Bay, but these sites are over 5 km from the fault. Unfortunately, no age control could be obtained immediately west of the fault because the first emergent terrace is only preserved for 1 km, and no marine deposits were observed along this section; west of here, the terrace is eroded back as the coastline curves inland, and no marine abrasion surfaces outcrop in the sea cliff for another ~5 km until WSAG. Thus, two possible ages from the highstand correlation are used to calculate a minimum and maximum differential uplift rate across the SBSYF. For this analysis, I use paleo-shoreline angle elevations from Rockwell et al. (1992) to eliminate any effects of changes in terrace width.

If the terrace is the same age across the SBSYF (45 ka), then the offset is a modest 4 m, resulting in a minimum differential uplift of 0.09 m/ky accommodated across the fault. This is about double the previously reported vertical slip rate, since the 45 ka terrace age is

~half the former 80 ka age (Rockwell et al., 1992). However, this scenario is unlikely because it would necessitate a further 16 m decrease in terrace shoreline elevation over the eroded interval to meet the 45 ka terrace when it re-emerges near WSAG at a lower elevation (Figure 9), and there are no structures present to accommodate this.

Given the updated terrace chronology, I propose a new interpretation, wherein the SBSYF juxtaposes terraces of different ages. Rather than a minor offset across the fault, followed by a gradual westward decline in terrace shoreline elevation over the ~5 km eroded interval (as mapped by Rockwell et al., 1992, Figure 2), I argue there is substantial displacement across the fault. In this case, the terrace on the east side of the fault is 45 ka, but it is not preserved immediately to the west of the fault because it has been eroded back. Instead, the terrace preserved for 1 km west of the fault is the 49.5 ka terrace. Thus, despite the relative continuity of the modern terrace elevations across the fault, there is a juxtaposition in terrace age across the fault—not a transition from MIS 3to MIS 5, but from 45 ka to 49.5 ka. Projecting the paleo-shoreline elevation of the 45 ka terrace from San Agustin Beach to the SBSYF (Figure 9) yields a 20 m offset in the same-age terrace across the fault. Consequently, this new interpretation yields a much higher differential uplift of up to 0.44 m/ky [(31-11 m)/45 ka] across the SBSYF. It is not possible to calculate a slip rate because the dip angle on the fault appears to vary, and the precise slip vector is unknown and likely has an oblique component.

Other faults could also be accommodating a portion of this shift in rock uplift rates. Notably, terrace elevations drop 20 m across the SBSYF and remain low to the west, unlike the short-wavelength displacements caused by other structures on the Gaviota Coast (i.e. More Ranch fault, Government Point Syncline) (Figure 9). Together with the changes in

qualitative geomorphic indicators of uplift observed in the Santa Ynez Mountains, this

marked and sustained decrease in terrace elevations suggests that regional structures with

longer-wavelength displacements are accommodating most of the coastal uplift. The Pitas

Point and the Santa Ynez faults are prime candidates, given their long mapped fault lengths

and appropriate senses of slip. Other offshore reverse faults, such as the Red Mountain fault

and Oak Ridge fault (Figure 2), taper out east of the Gaviota Coast or have the up-thrown

block on the south side. Yet, the observed knickpoint in the longitudinal profile of Gaviota

Creek and shift from alluvial to bedrock channel conditions serve as independent evidence

that the SBSYF is also active, with a south-side up component of slip. Given these lines of

reasoning, I interpret the 0.44 m/ky decrease in rock uplift to be related to the Pitas Point

Fault or Santa Ynez Faults at the first order, and the SBSYF at the second order. The

SBSYF may be interacting with or affecting the Pitas Point and Santa Ynez faults at depth,

and could behave as a tear fault accommodating the observed westward decline in

shortening. Nonetheless, the SBSYF evidently acts as a structural boundary that separates

high- and low-uplift tectonic segments of the Gaviota Coast.

The results from this study reinforce the idea that rock uplift rates derived from

marine terraces are regional rates of uplift: they do not reflect displacement from any one

fault or fault, but rather the net accumulation of displacement from multiple structures. The

spatial distribution of rock uplift rates relative to mapped structures on the Gaviota Coast

indicates that coastal uplift is a combination of long-wavelength, regional uplift sourced

from larger, deep-rooted structures (such as the Santa Ynez fault and offshore Pitas Point

fault), which is then overprinted and locally modified by smaller, shallow structures that

only cause short-wavelength displacement.

Holocene platforms

The possibility of Holocene terraces in the Santa Barbara region is an outstanding question. This prospect received additional attention after Rockwell et al. (2016) reported them at Pitas Point near Ventura. Upson (1951) made an early case for low altitude paleo-shorelines along the Gaviota Coast, describing several notches, benches, and emergent platforms up to 7 feet "above the high-tide water level" or "above the beach." Although Holocene terraces are not the focus of this study, I scrutinized the coastline for evidence of low elevation platforms during fieldwork. These observations are discussed below.

Small benches in the bedrock (<1 m tall) occasionally occur adjacent to the sea cliff (Figure 12a). These features extend about 1-3 m from the sea cliff, and are typically not laterally extensive, though in places they are almost 100 m wide (i.e. east of Naples Point). Notably, the benches only appear when bedding strikes parallel to the shoreline. When bedding is oblique to the shoreline, erosion-resistant strata can be unmistakably recognized protruding from the sea cliff at an angle (Figure 12b). These observations suggest that rather than erosional remnants of a recently uplifted bedrock platform, these bench features are simply the remains of competent beds at the foot of an actively retreating sea cliff.

Excluding the Pleistocene terraces at the focus of the study, no wave-cut features were observed above the high tide line. The author investigated supposedly emergent platforms at Cañada del Corral and Arroyo Hondo reported by Upson (1951), but it was clear from the presence of standing water, living algae and anemone, and damp sand with wave ripples that these features are not in fact above the high tide water line. Indeed, aerial imagery on Google Earth confirmed these sites have been completely inundated on numerous occasions (i.e. 12/2014, 10/2006). Rather than a distinct beveled platform, these

features more closely resemble discontinuous beds of indurated shale outcropping from the beach sand (Figure 13).

At Arroyo Hondo, the geometry and geology of the site indicate the feature is not an uplifted Holocene terrace. If the apparent platform were uplifted by a shore-parallel fault, then the emergent beds would be expected to extend all the way to the modern sea cliff. However, at Arroyo Hondo there are gaps between the exposed bedding and the sea cliff (Figure 13). If the apparent platform were uplifted by a fault striking oblique to the shoreline, a sudden truncation or disappearance of the platform would be expected to one side. Instead, to the west the beds gradually peter out and fall below sea level, and to the east the beds trend directly into the sea cliff. Lastly, anticlinal upwarping is unlikely because the bedrock surrounding Arroyo Hondo dips uniformly to the south (Dibblee, 1988). Similar to the apparent benches adjacent to the sea cliff, these observations suggest that this feature is not an uplifted Holocene terrace, but simply a function of differential weathering of the Monterey Formation on the modern wave-cut platform.

Another conspicuous low-elevation feature to consider is a ~200 m planar platform near Devereux Lagoon that rises 2 m+ above the beach (Figure 14a). If this platform were in fact a Holocene terrace, beneath the modern terrestrial cover one would expect to find a beveled marine abrasion surface cut into bedrock, much like the Pleistocene terraces (Figure 14b). However, cross-section exposures of the platform from gullies cut by the winter storms of 2017 show that there is no intact bedrock at the base of platform. Instead, the platform consists of poorly consolidated sediments resembling artificial fill: a matrix-supported breccia with gravel- to cobble-sized angular clasts of white, low density, extremely friable diatomaceous shale, with a medium sand matrix, and occasional larger

blocks of the diatomaceous shale over 50 cm on the long-axis (Figure 14c). Moreover, the

diatomaceous material does not seem to be locally derived because it differs substantially

from the Sisquoc Shale exposed in the sea cliff directly behind the platform (Figure 14b).

These observations demonstrate that the platform near Devereux Lagoon is not a Holocene

terrace. Instead, it is likely an anthropogenic feature—potentially an old road that was built

to access the nearby oil facilities just to the west. In summary, despite the relatively high

uplift rates along the Gaviota Coast reported in this study, neither fieldwork nor remote

imagery analyses yielded any definitive signs of uplifted Holocene platforms.

### *Implications for earthquake hazard assessments*

Given that rock uplift rates along the Gaviota Coast are higher than previously

thought, this has important implications for seismic hazard. Records of two strong historical

earthquakes (estimated magnitudes 7.1 and 6.8; Sylvester, 2001) and the 100+ km mapped

lengths of the Pitas Point and Santa Ynez faults indicate that regional M 7+ earthquakes are

possible (Wells and Coppersmith, 1994). Faster uplift rates could mean earthquake

recurrence intervals are shorter, or that faults on the western Gaviota Coast are more likely

to be involved in long fault ruptures in the Santa Barbara Fold Belt. Because recurrence

interval and fault rupture length are both key factors in seismic risk (Youngs and

Coppersmith, 1985), this could lead to heightened seismic risk for the Santa Barbara region.

Yet, this study also provides evidence for structural segmentation of the Gaviota

Coast at the SBSYF. If segmentation localizes fault ruptures to smaller segments, then

higher uplift rates may not necessarily lead to greater seismic hazard. Moreover,

quantification of seismic hazard is based on fault slip rates, not time-averaged regional uplift

rates. Although further work is needed to estimate fault slip rates and identify precisely

which faults are accommodating most of the coastal uplift, the rock uplift rates reported in this study provide much-needed constraints that will inform regional tectonic models and future assessments of seismic hazard.

CONCLUSIONS

New radiocarbon and optical ages indicate the first emergent terrace on the Gaviota Coast formed during MIS 3. This includes the western Gaviota Coast, which was previously thought to be 80 ka. Updated terrace chronology yields time-averaged rock uplift rates between 0.9-2.0 m/ky, which are over five times higher than prior estimates. Coastal uplift is the net sum of long-wavelength uplift from deep, regional structures, with local deviations controlled by smaller, shallower structures. The SBSYF forms a structural boundary between two segments of the coastline, with lower terrace elevations and rock uplift rates (~1.1 m/ky) occurring on the western Gaviota Coast, and higher rates (~1.5 m/ky) to the east, though lower rates occur locally at Isla Vista (~1 m/ky). The SBSYF is confirmed to be active, with a south-side up component of slip, as evidenced by a knickpoint in the longitudinal profile of Gaviota Creek and a shift from alluvial to bedrock channel conditions downstream of the fault. Sustained low terrace elevations west of the SBSYF suggest a regional fault accommodates most of the differential uplift along the Gaviota Coast.
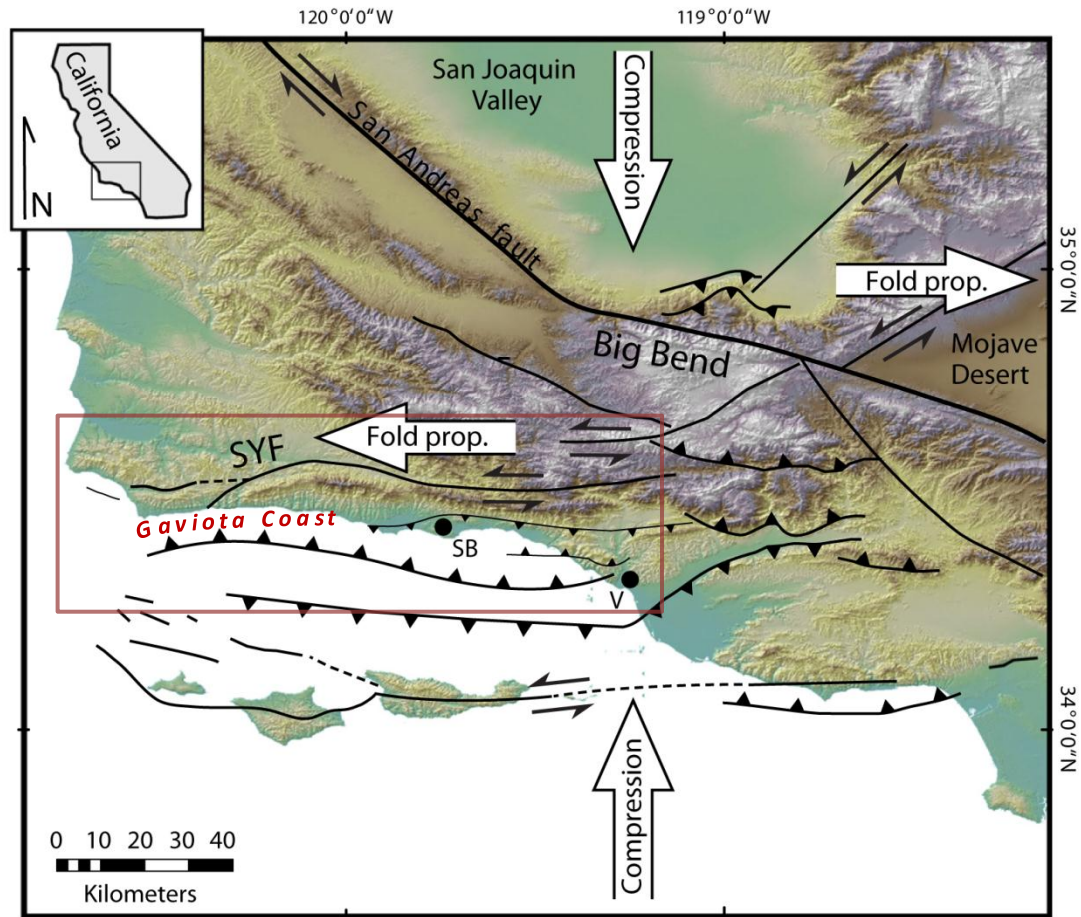
Figure 1 Tectonic setting of the Western Transverse Ranges Province in southern California. North-south crustal shortening associated with the Big Bend in the San Andreas fault is accommodated by the growth of east-west trending mountain ranges, folds, and faults. The red box outlines the extent of Figure 2. SB—Santa Barbara; V—Ventura; SYF—Santa Ynez fault. Modified from Keller and DeVecchio, 2013.
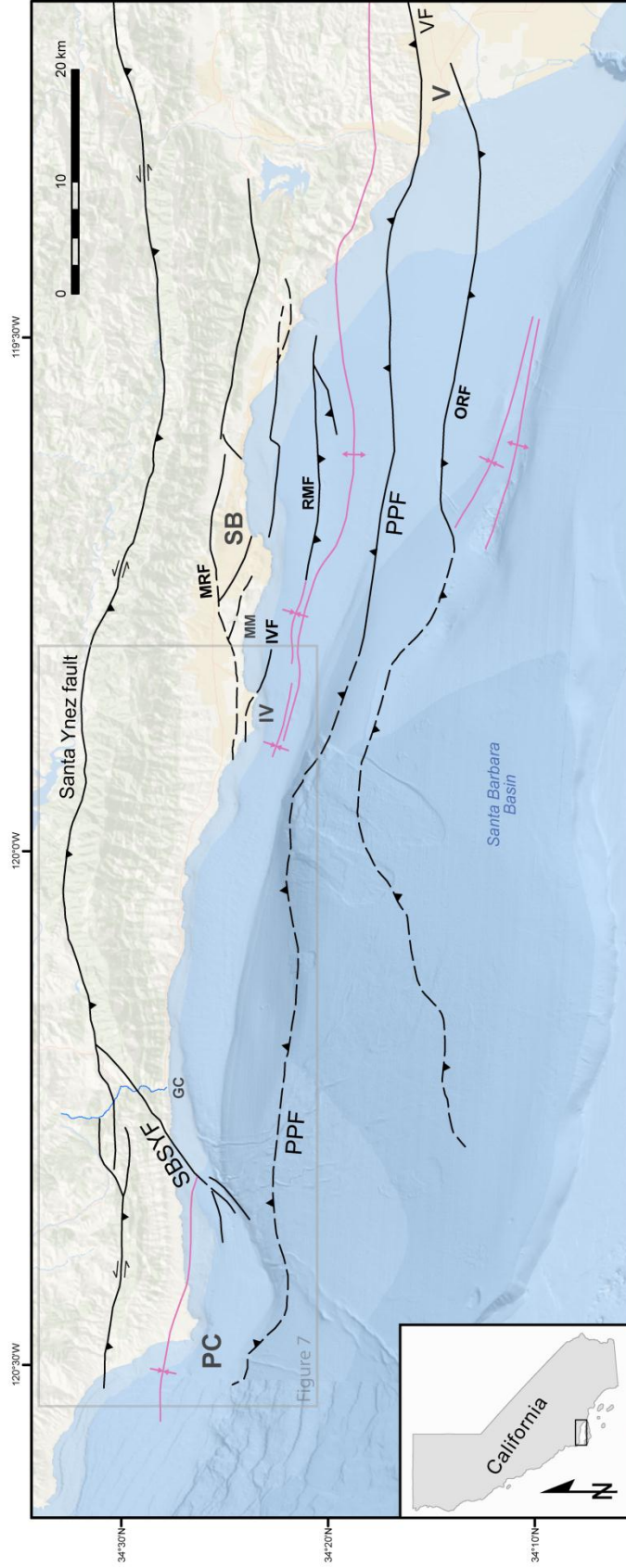
Figure 2 Map of the Santa Barbara coastal region with major structures mapped on and offshore. Structural information from Johnson et al. (2017), basemap from ESRI. Abbreviations: GC—Gaviota Creek; IV—Isla Vista; IVF—Isla Vista fault; MM—More Mesa; MRF—More Ranch fault; ORF—Oak Ridge fault; PC—Point Conception; PPF—Pitas Point fault; RMF—Red Mountain fault; SB—Santa Barbara; SBSYF—South Branch Santa Ynez fault; SYM—Santa Ynez Mountains; V—Ventura; VF—Ventura fault.
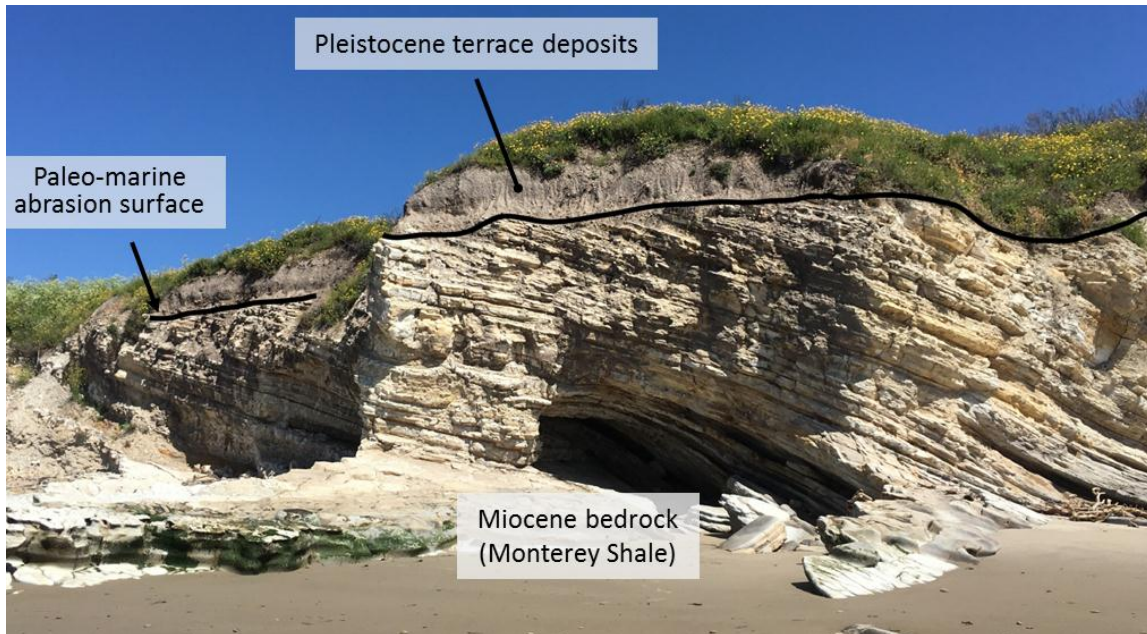
Figure 3 Characteristic marine terrace exposure in the modern sea cliff. Moderately dipping Miocene bedrock is truncated by the paleo-marine abrasion surface, and unconformably overlain by sub-horizontal Pleistocene terrace deposits, which consist of marine sands locally (not pictured) and alluvium. Photo taken ~1 km east of Refugio State Beach.
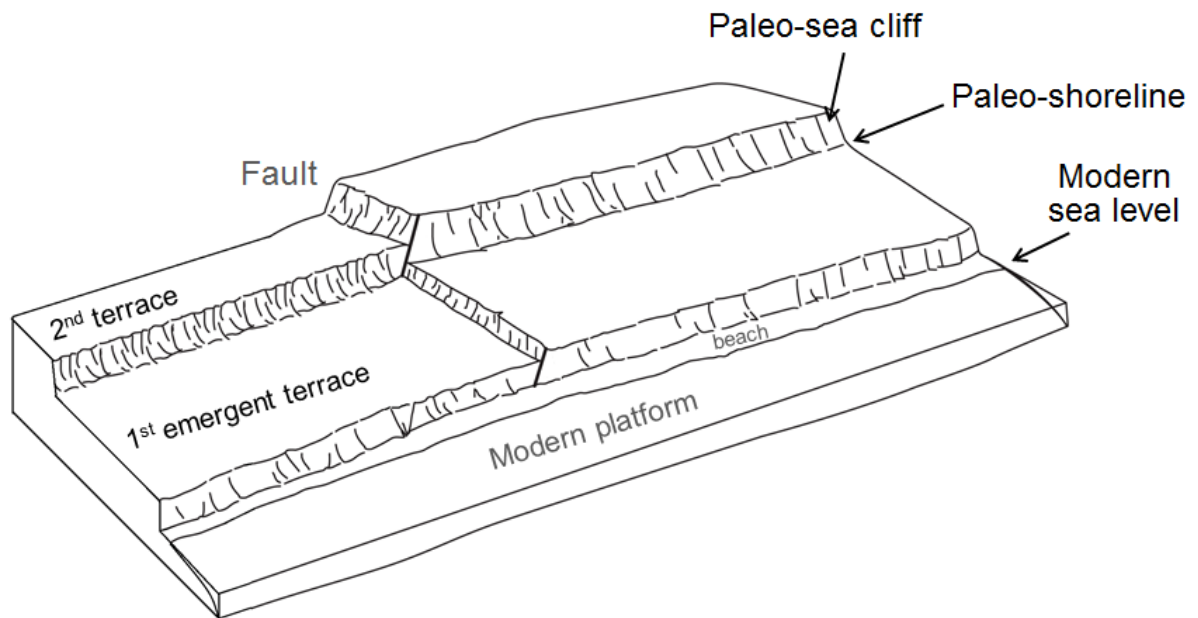

Figure 4 Idealized diagram of a flight of marine terraces, with modern platform, illustrating the terrace morphology and key features (modified from Trecker et al., 1998).
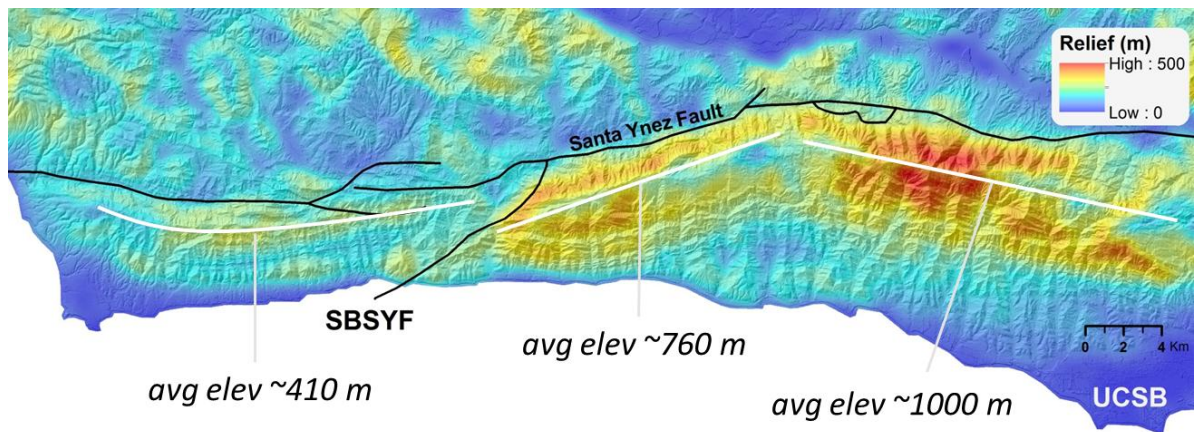
Figure 5 Topographic relief and mean crest-line elevations of the Santa Ynez Mountains, which are split into geomorphic segments. The mean elevation of each segment increases to the east, and appears to be structurally controlled. Topographic relief calculated using a 500 m-radius moving circle. Mean crest-line elevations from Keller and DeVecchio (2013).
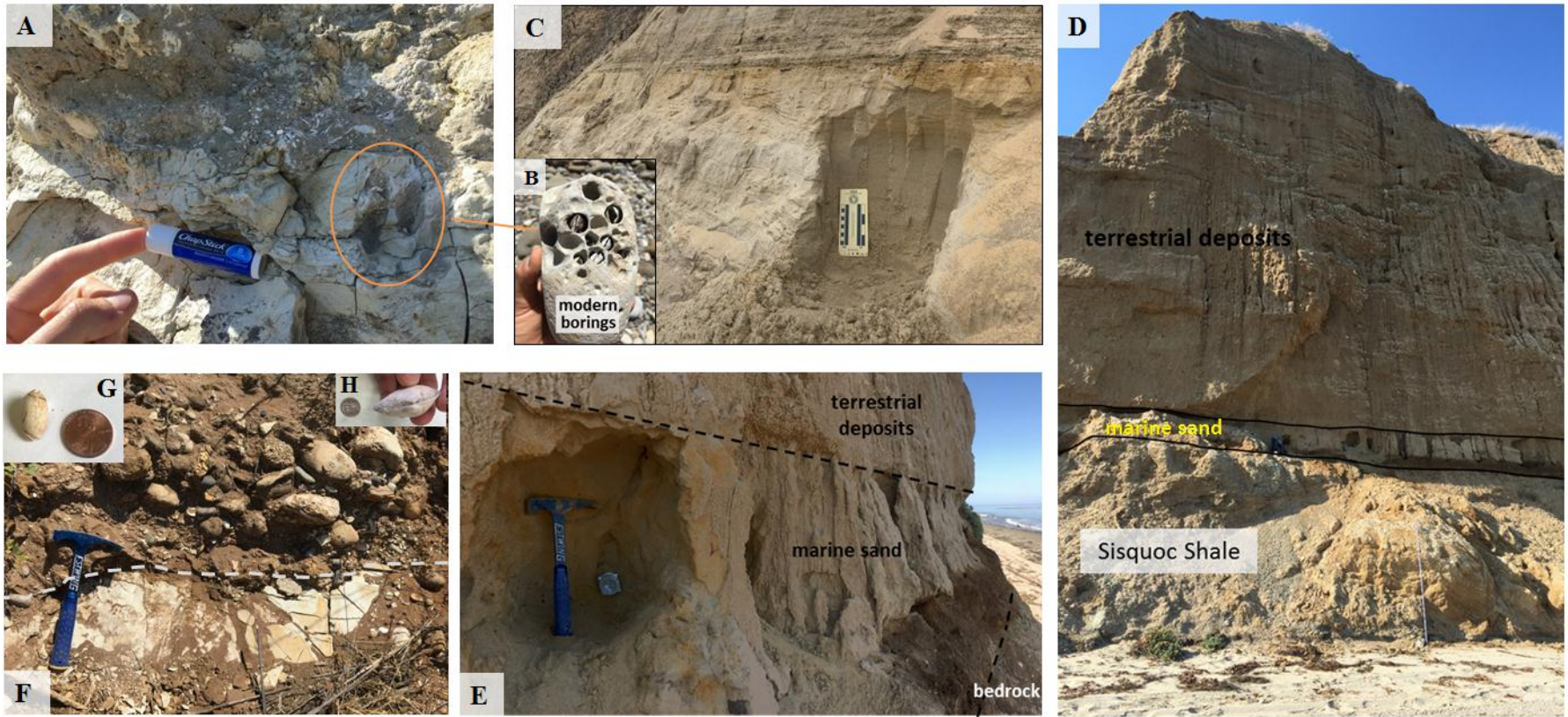
Figure 6 Field photos of radiocarbon and OSL sample sites in sea cliff exposures. (A) Shell hash layer with in-filled pholad borings circled at ENP; (B) modern beach cobble with pholad borings; (C) well-sorted marine sand with parallel laminations at WNP; (D,E) marine terrace sands form a distinct layer at WSAG, with OSL sample tube in E; (F) cobble layer with shelly matrix overlying the paleo-marine abrasion surface at WGV; (G) *Olivella biplicata*, WLV; and (H) articulated *Macoma inquinata*, EBC.
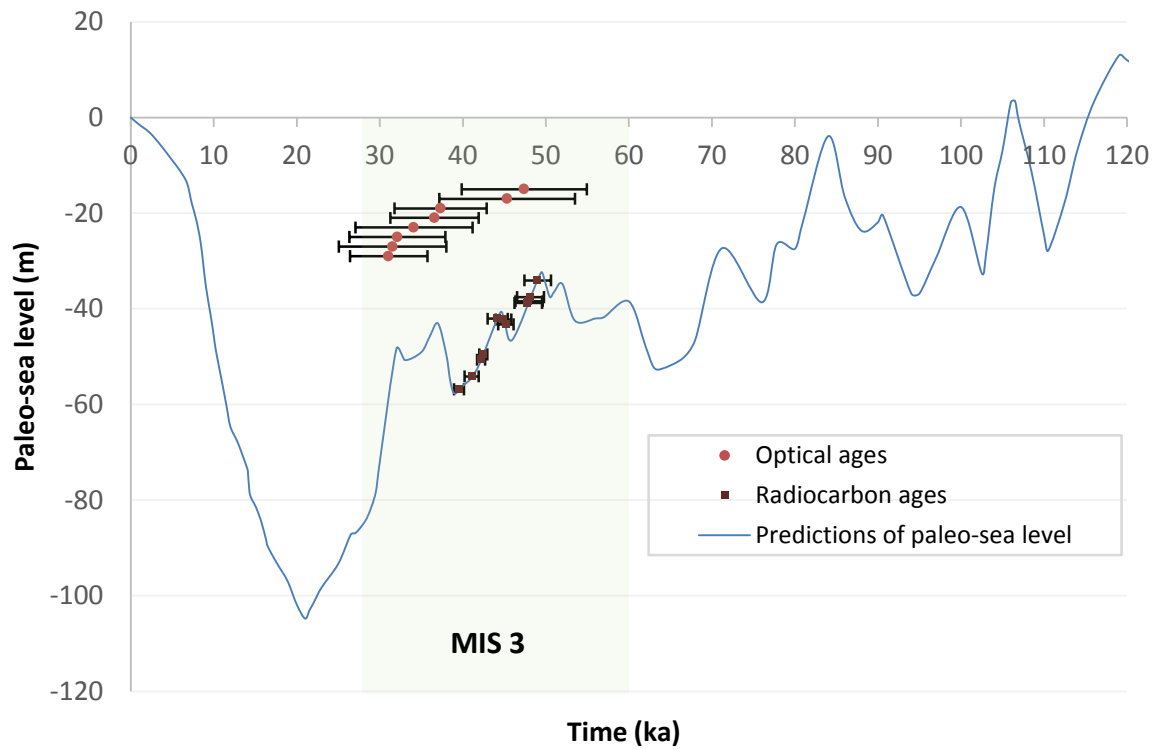
Figure 7 Sample ages for the first emergent terrace plotted with a GIA-adjusted sea level curve (Simms et al., 2016) for the latitude of Gaviota, CA. Calibrated radiocarbon ages are projected onto the curve based on paleo-sea level at the time. The optical ages are included for reference, but the y-axis is arbitrary. The time axis is the same for all data shown. The green box encompasses the date range of marine isotope stage 3.
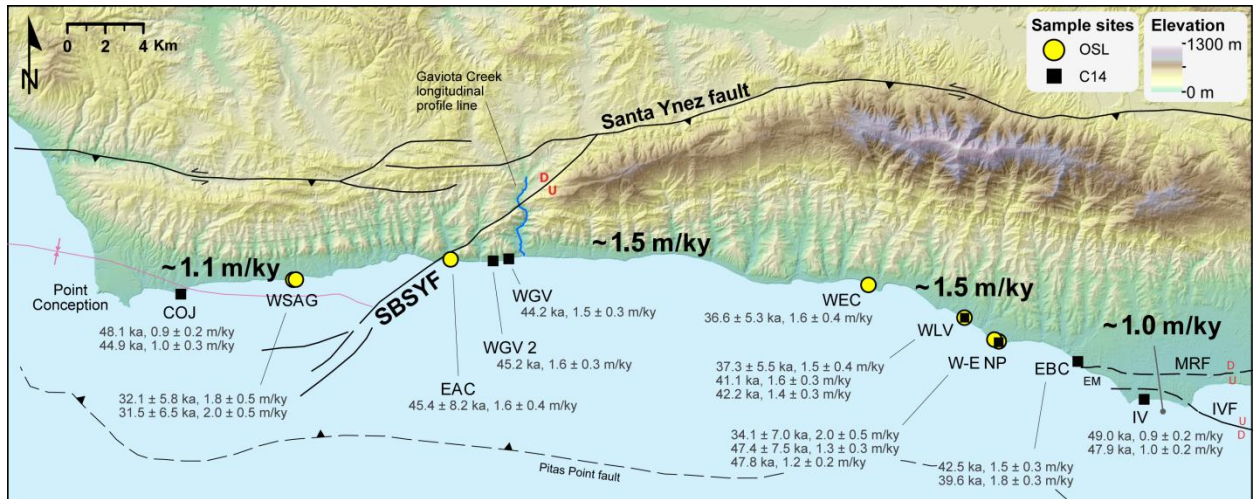
Figure 8 Sample site locations along the Gaviota Coast, with regional time-averaged rock uplift rates shown in bold; note the lower rates on the western Gaviota Coast and at Isla Vista. Ages and rock uplift rates from individual sites are shown in gray text, with 2σ errors for optical ages and median calibrated ages for radiocarbon samples (for complete calibrated age ranges, see Table 1). Sample abbreviations refer to site locations in Tables 1 and 4. Other abbreviations: EM—Ellwood Mesa; IVF—Isla Vista fault; MRF—More Ranch fault; SBSYF—South Branch Santa Ynez fault.
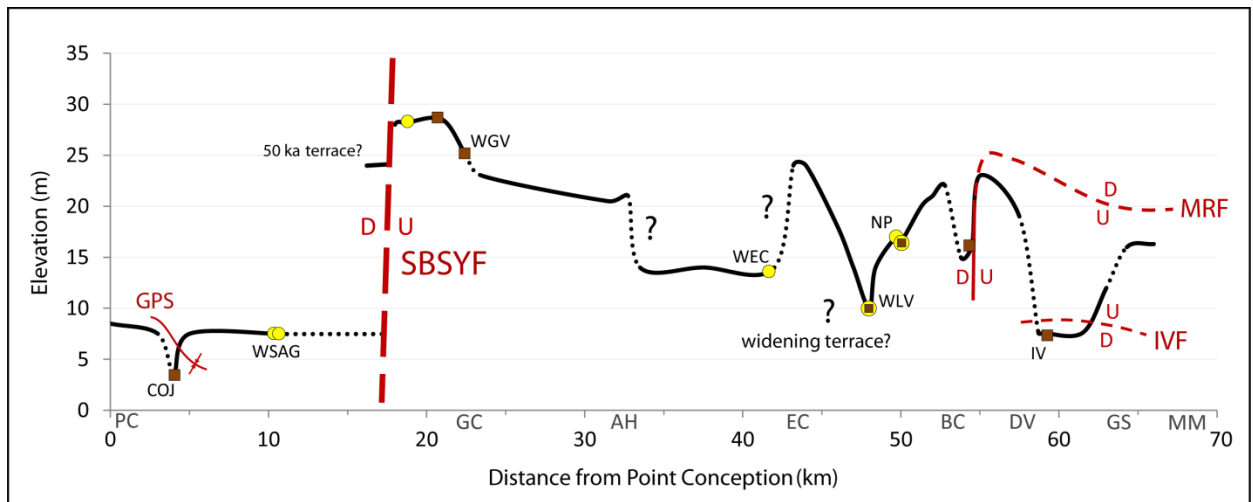

Figure 9 Along-shore profile of paleo-marine abrasion surface elevations exposed in the sea cliff of the first emergent terrace, dotted where the terrace is missing due to fluvial erosion or sea cliff retreat (i.e. west of SBSYF). Geochronology sample locations and relevant structures locally deforming the terrace are also shown. Although the elevation of the paleo-marine abrasion surface can change with variations in terrace width (due to the ~1 degree seaward slope of the bedrock platform), the Gaviota Coast has a consistent east-west trend, so it is generally apparent where a substantial change in terrace width is responsible for a shift in the abrasion surface elevation (i.e. between EC and WLV). Sample abbreviations refer to those in Tables 1 and 4. Other abbreviations: AH—Arroyo Hondo, BC—Bell Canyon, DV—Devereux Slough, EC—El Capitan Creek, GC—Gaviota Creek, GS—Goleta Slough, GPS—Government Point Syncline, IVF—Isla Vista Fault, MM—More Mesa, MRF—More Ranch Fault, PC—Point Conception.
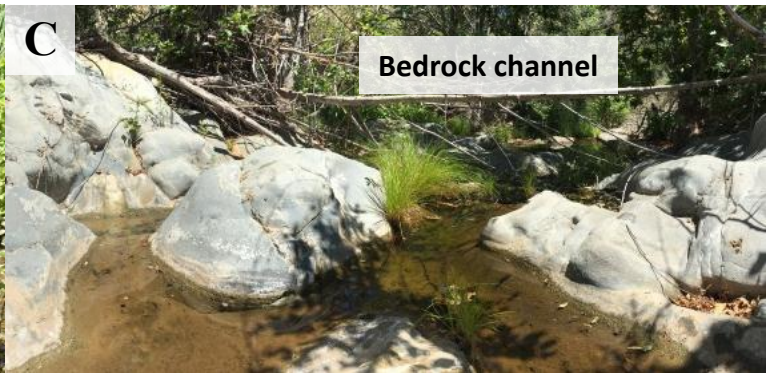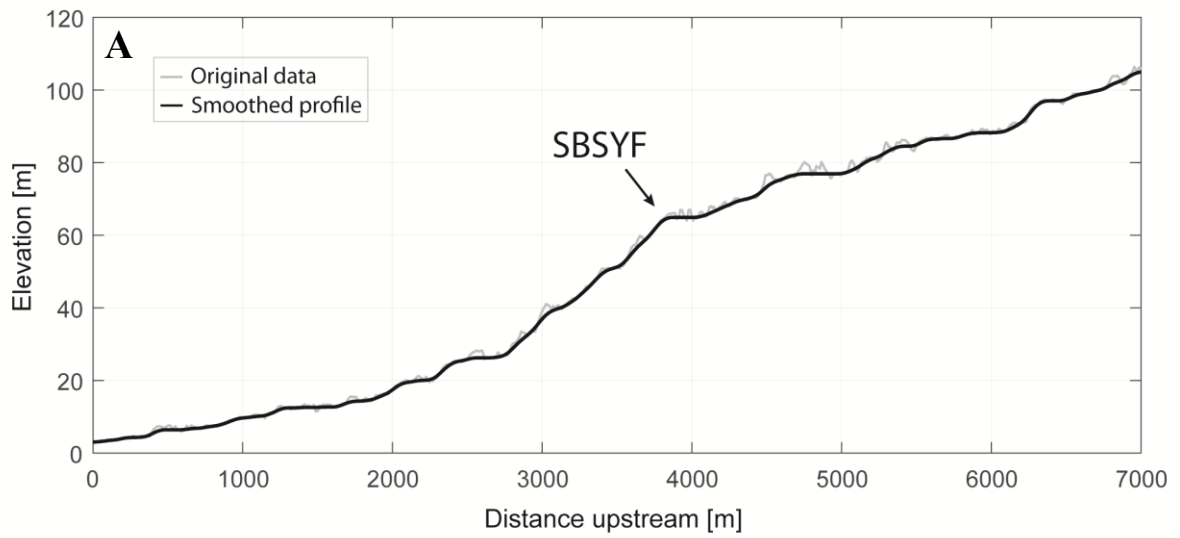
Figure 10 (A) Longitudinal profile of Gaviota Creek, with a distinct knickpoint as the stream crosses the SBSYF, indicating an axis of active uplift. (B) Alluvial channel just upstream of where Gaviota Creek crosses the SBSYF. (C) Bedrock channel just downstream of the fault crossing.
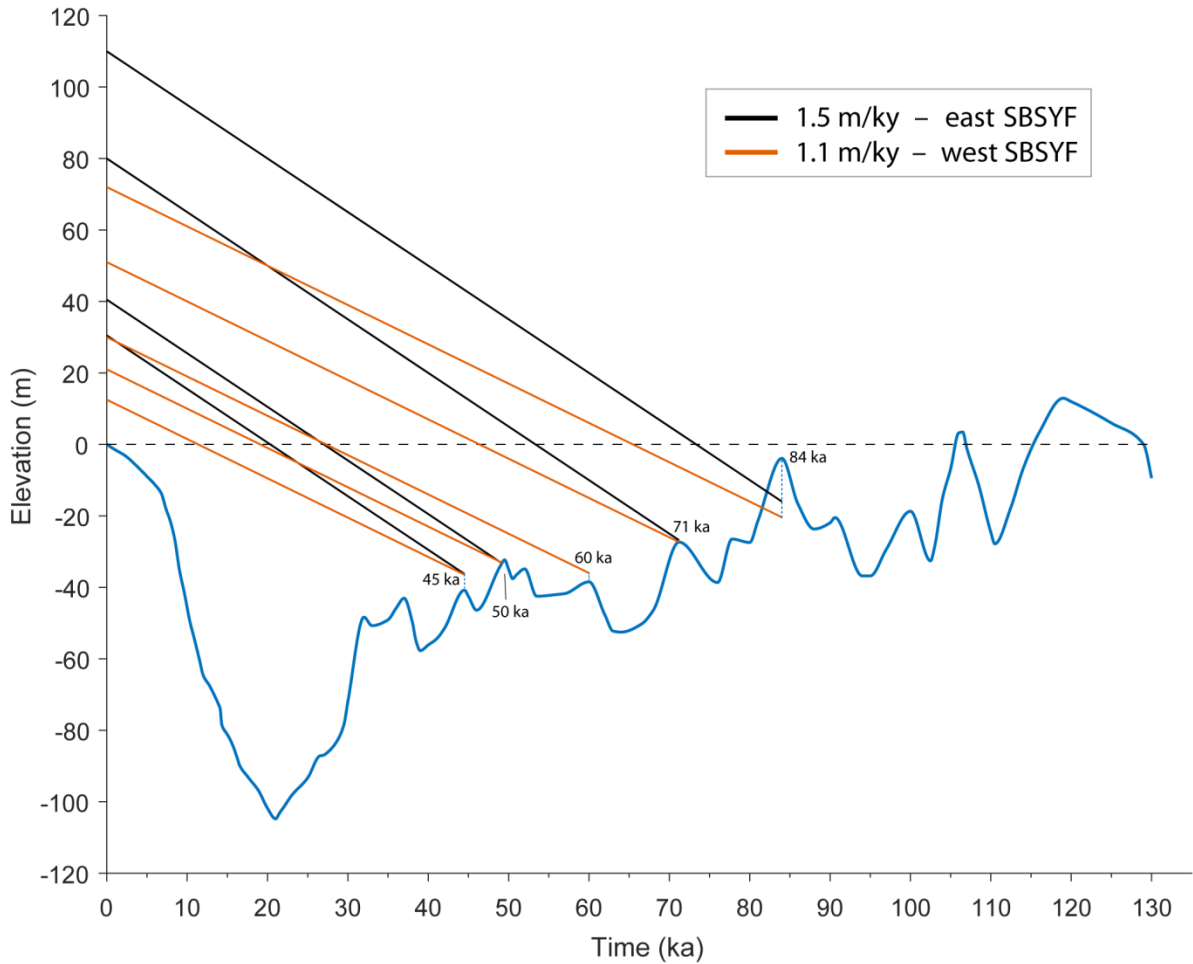
Figure 11 Two sets of paleo-shoreline elevations from a flight of marine terraces offset by the SBSYF are correlated to sea level highstands, based on projections of time-averaged rock uplift rates. The terraces on the east side of the SBSYF (black lines) are at higher elevations due to a faster uplift rate, but pairs of same-age terraces still converge at the same highstands. Note that the 4th terrace (60 ka) is not preserved on the east side of the SBSYF, so this highstand is only associated with one projected uplift path. GIA-adjusted sea level curve from Simms et al. (2016) and paleo-shoreline elevations from Rockwell et al. (1992).
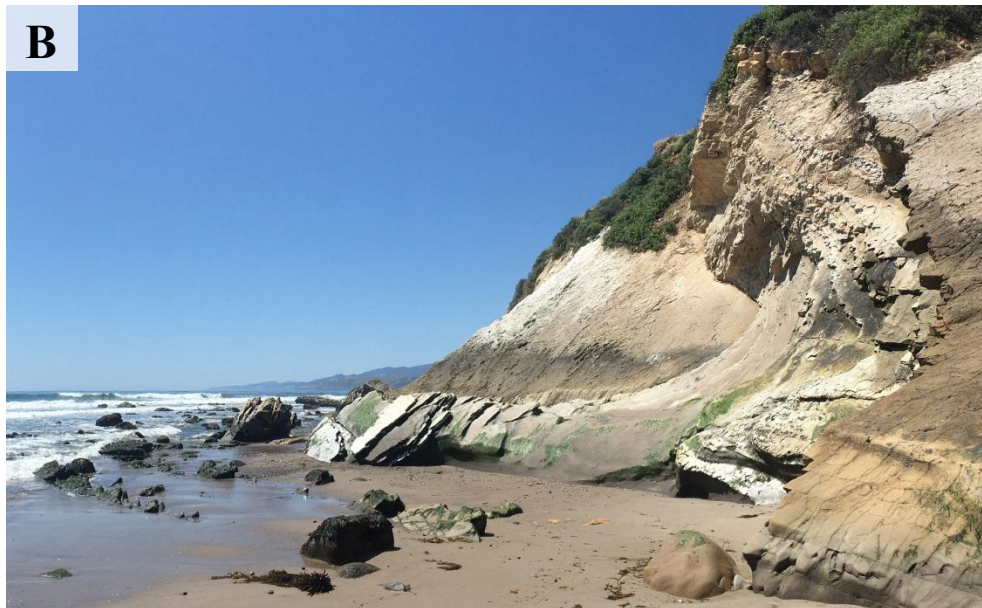
Figure 12   (A) A conspicuous ~80 cm tall bench at the foot of the sea cliff east of Naples Point, where bedding strikes parallel to the shoreline. (B) Erosion-resistant beds in the Monterey Shale strike oblique to the shoreline, forming an isolated raised bed that protrudes from the sea cliff. This pair of photos demonstrates how such resistant beds can form an apparent bench and potentially be mistaken for an emergent platform if they happen to strike parallel to the sea cliff.

Figure 13 Beds of the Monterey Shale formation exposed at Arroyo Hondo, interpreted to be a result of differential weathering of the modern wave-cut platform, rather than an uplifted Holocene platform. The beds strike offshore in the background and are submerged. In the foreground, the beds (as well as the above Pleistocene terrace) are truncated due to fluvial erosion from the Arroyo Hondo drainage. Note the gaps between the exposed beds and the sea cliff in the background framed by the white box (see text for details).

Figure 14   Beach and outcrop photos from Ellwood Mesa, ¾ km west of Devereux Slough. (A) Landscape view of the conspicuous platform ~2 m above the beach in the foreground, with the higher Pleistocene terrace in the background. (B) Nearby sea cliff exposure of the ~18 m Pleistocene terrace, with paleo-marine abrasion surface cut into the fractured, but intact Sisquoc Shale bedrock. (C) Gully exposure of the lower platform, revealing artificial fill all the way down to the modern beach elevation. A Holocene marine terrace would exhibit a similar geometry to (B), but there is no intact bedrock or paleo-marine abrasion surface present, suggesting a different origin for this feature.

Table 1 Radiocarbon ages of marine mollusks samples collected from the first emergent terrace along the Gaviota Coast, and the corresponding time-averaged rock uplift rates derived from these ages. Samples are listed from west to east along the coast.

Site ID	Site location	Sample genus	Description	Radiocarbon age (RCYBP)	Calibrated age range B.P. (2σ)*	Peak probability (ky B.P.)	Sample elevation (m)	Paleo-sea level§ (m)	Uplift rate (m/ky)
COJ 1	Cojo Bay 1	*Lucinisca*	Inarticulated	45,540 ± 740	46,533–49,780	48.1	4.1 ± 1.5	-38 ± 11	0.9 ± 0.2
COJ 2	Cojo Bay 2	*Tellina*	Inarticulated	42,220 ± 510	43,968–45,831	44.9	4.1 ± 1.5	-42 ± 11	1.0 ± 0.3
WGV 2	W. Gav. Canyon2	*Macoma*	Inarticulated	42,550 ± 520	44,268–46,120	45.2	28.6 ± 1	-43 ± 11	1.6 ± 0.3
WGV	W. Gav. Canyon	*Olivella*	Worn shell	41,400 ± 730	42,986–45,432	44.2	25.1 ± 1	-42 ± 11	1.5 ± 0.3
WLV 1	W. Las Varas 1	*Olivella*	Pristine shell	38,690 ± 330	41,731–42,671	42.2	10.3 ± 1	-51 ± 11	1.4 ± 0.3
WLV 2	W. Las Varas 2	*Platydon*	Articulated	37,270 ± 450	40,210–41,910	41.1	10.3 ± 1	-54 ± 11	1.6 ± 0.3
WLV 3	*W. Las Varas 3*	*Platydon*	*Inarticulated*	*48,900 ± 1100*	*n/a*[#]	*n/a*	*10.3 ± 1*	*n/a*	*n/a*
ENP	E. Naples Point	Bivalve	Shell hash	45,270 ± 740	46,227–49,545	47.8	17.2 ± 0.5	-39 ± 11	1.2 ± 0.2
EBC 1	E. Bell Canyon 1	*Macoma*	Articulated	39,110 ± 340	41,990–42,936	42.5	16.2 ± 1	-50 ± 11	1.5 ± 0.3
EBC 2	E. Bell Canyon 2	*Macoma*	Articulated	35,760 ± 230	38,940–40,146	39.6	16.2 ± 1	-57 ± 11	1.8 ± 0.3
IV 1	Isla Vista 1	*Platydon*	In-situ, artic.	46,520 ± 840	47,409–50,000[†]	49.0	7.6 ± 0.5	-34 ± 11	0.9 ± 0.2
IV 2	Isla Vista 2	*Platydon*	In-situ, artic.	45,350 ± 730	46,324–49,606	47.9	7.6 ± 0.5	-38 ± 11	1.0 ± 0.2

*Calibrated age ranges are reported in years before 2017 (B.P). All calibrations made using the Calib program v7.1 (Stuiver and Reimer, 1993; Stuiver et al., 2017) with the MARINE13 curve (Reimer et al., 2013). All marine samples used a ΔR (marine reservoir correction factor) of 328±40, based on the mean of the two nearest pre-bomb modern marine shell dates located offshore of downtown Santa Barbara (Ingram and Southon, 1996). No other marine specimens were available within ~40 km. Estuarine samples were avoided because they can have variable ΔR values (Holmquist et al., 2015).

§Paleo-sea level at time of deposition based on radiocarbon ages and a GIA-corrected sea level curve by Simms et al. (2016), generated for the latitude of Gaviota, CA . Uncertainty was derived from the full range of sea level curves made by all of the Earth mantle and ice volume models that were considered in the development of the published curve. Paleo-sea level is reported relative to modern sea level.

#This radiocarbon age is too old to be calendar calibrated, and was excluded from analysis. The sample is likely an older, recycled shell fragment that does not reflect time of deposition or platform cutting.

†The calibrated age range maxed out at 50 ka, the upper limit of the age model, but the sample was young enough for the Calib program to generate a peak probability for the sample.

Table 2 Terrace chronology comparison between this study and Gurrola et al. (2014) at overlapping sample sites on the eastern Gaviota Coast, showing agreement of radiocarbon ages with other methods.

	This study		Gurrola et al. (2014)	
Site Location	Calibrated Radiocarbon Age Range B.P. (2σ)[1]	Peak Probability (ky B.P.)	OSL age (ka)	U-series age on coral (ka)
E. Bell Canyon 1	41,990–42,936	42.5	45 ± 4	
E. Bell Canyon 2	38,940–40,146	39.6	36 ± 3	
Isla Vista 1	47,409–50,000[†]	49.0		49 ± 1.7
Isla Vista 2	46,324–49,606	47.9		47 ± 0.5

Table 3 Dose rate information for optically stimulated luminescence ages.

Site ID	Site location	Grain size (μm)	In-situ (H20) %[*]	K (%)[§]	Rb (ppm)[§]	Th (ppm)[§]	U (ppm)[§]	Cosmic (Gy/ky)
WSAG_osl1	W. San Augustine Beach 1	150-250	1.9	2.04 ± 0.05	69.7 ± 2.8	12.7 ± 1.1	2.4 ± 0.2	0.04 ± 0.00
WSAG_osl2	W. San Augustine Beach 2	150-250	2.9	2.36 ± 0.06	80.8 ± 3.2	13.5 ± 1.2	2.8 ± 0.2	0.04 ± 0.00
EAC_osl	E. Alegria Canyon	150-250	5.9	2.33 ± 0.06	82.9 ± 3.3	5.4 ± 0.5	2.0 ± 0.1	0.14 ± 0.01
WEC_osl	W. El Capitan	150-250	4.7	2.99 ± 0.07	98.5 ± 3.9	3.3 ± 0.3	2.2 ± 0.2	0.07 ± 0.01
WLV_osl	W. Las Varas Canyon	125-212	6.1	2.96 ± 0.07	100.5 ± 4.0	4.4 ± 0.4	1.1 ± 0.1	0.08 ± 0.01
WNP_osl	W. Naples Point	150-250	2.6	2.54 ± 0.06	82.1 ± 3.3	3.6 ± 0.3	1.0 ± 0.1	0.12 ± 0.01
ENP_osl2	E. Naples Point 2	150-250	0.7	2.30 ± 0.06	71.2 ± 2.8	4.4 ± 0.4	1.2 ± 0.1	0.13 ± 0.01
ENP_osl1	E. Naples Point 1	150-250	1.3	2.37 ± 0.06	80.2 ± 3.2	3.6 ± 0.3	1.1 ± 0.1	0.12 ± 0.01

*Assumed 5.0 ± 2.0% for samples with in-situ values <5% for moisture content over burial history.
[§]Radioelemental concentrations determined by ALS Chemex using ICP-MS and ICP-AES techniques.

Table 4 Optical ages of raised beach sands sampled from the first emergent terrace along the Gaviota Coast, and the corresponding time-averaged rock uplift rates derived from these ages. Samples are listed from west to east.

Site ID	Site location	Number of aliquots[1]	Dose rate[2] (Gy/ky)	Equivalent dose[3] ± 2σ (Gy)	Optical age ± 2σ (ka)	Sample elevation (m)	Paleo sea level[4] (m)	Uplift rate (m/ky)
WSAG_osl1	W. San Augustine Beach 1	19 (30)	3.31 ± 0.16	106.25 ± 16.05	32.13 ± 5.78	8.1 ± 1.5	-49 ± 11	1.8 ± 0.5
WSAG_osl2	W. San Augustine Beach 2	18 (26)	3.75 ± 0.18	118.21 ± 21.34	31.54 ± 6.48	8.4 ± 1.5	-54 ± 11	2.0 ± 0.5
EAC_osl	E. Alegria Canyon	18 (32)	3.08 ± 0.14	139.85 ± 21.08	45.35 ± 8.17	30.2 ± 0.5	-44 ± 11	1.6 ± 0.4
WEC_osl	W. El Capitan	18 (28)	3.57 ± 0.15	130.58 ± 13.79	36.59 ± 5.31	14.3 ± 0.5	-44 ± 11	1.6 ± 0.4
WLV_osl	W. Las Varas Canyon	19 (25)	3.36 ± 0.14	125.59 ± 13.76	37.33 ± 5.54	11.7 ± 1.0	-45 ± 11	1.5 ± 0.4
WNP_osl	W. Naples Point	15 (19)	2.95 ± 0.13	100.63 ± 18.14	34.12 ± 7.04	18.5 ± 1.5	-50 ± 11	2.0 ± 0.5
ENP_osl2	E. Naples Point 2	20 (29)	2.83 ± 0.12	134.16 ± 16.69	47.41 ± 7.54	18.8 ± 0.5	-41 ± 11	1.3 ± 0.3
ENP_osl1	*E. Naples Point 1*	*20 (40)*	*2.81 ± 0.12*	*87.35 ± 9.84*	*31.07 ± 4.67**	*18.4 ± 0.5*	*N/A*	*N/A*

[1]Number of aliquots used in age calculation and number of aliquots analyzed in parentheses.
[2]Dose rates derived from radioelemental concentrations by conversion factors from Guérin et al. (2011). See Table 3 for dose rate details.
[3]Equivalent dose calculated using the Central Age Model of Galbraith and Roberts (2012).
[4]Paleo-sea level at time of deposition based on radiocarbon ages and a GIA-corrected sea level curve by Simms et al. (2016), generated for the latitude of Gaviota, CA . Uncertainty was derived from the full range of sea level curves made by all of the Earth mantle and ice volume models that were considered in the development of the published curve. Paleo-sea level is reported relative to modern sea level.
*Italicized sample excluded from analysis. See text for details.

REFERENCES

Aitken, M. J., 1998, Introduction to optical dating: the dating of Quaternary sediments by the use of photon-stimulated luminescence. Clarendon Press.

Bloom, A.L., Broecker, W.S., Chappell, J.M.A., Matthews, R.K., and Mesolella, K.J., 1974, Quaternary sea level fluctuations on a tectonic coast: New Th-230/U-234 dates from the Huon Peninsula, New Guinea: Quaternary Research, v. 4, p. 185–205.

Bradley, W.C., 1957, Origin of Marine-terrace deposits in the Santa Cruz area, California: Bulletin of the Geological Society of America, v. 68, p. 421–444.

Bradley, W.C., and Addicott, W.O., 1968, Age of first marine terrace near Santa Cruz, California: Geological Society of America Bulletin, v. 79, p. 1203–1210.

Bradley, W.C., and Griggs, G.B., 1976, Form, genesis, and deformation of central California wave-cut platforms: Bulletin of the Geological Society of America, v. 87, p. 433–449, doi: 10.1130/0016-7606(1976)87<433:FGADOC>2.0.CO;2.

Broecker, W.S., Thurber, D.L., Goddard, J., Ku, T.L., Matthews, R.K., and Mesolella, K.J., 1968, Milankovitch hypothesis supported by precise dating of coral reefs and deep-sea sediments: Science, v. 159, p. 297–300, doi: 10.1126/science.159.3812.297.

Bull, W.B., 1985, Correlation of flights of global marine terraces, *in* Morisawa, M., and Hack, J., eds., Tectonic Geomorphology: Proceedings, Binghamton Geomorphology Symposium, 15th, Binghamton, New York, September 1984, Allen and Unwin, p. 129–152.

Bull, W.B., and Cooper, A.F., 1986, Uplifted marine terraces along the Alpine fault, New Zealand: Science, v. 234, p. 1225–1228.

Burbank, D.W., McLean, J.K., Bullen, M., Abdrakhmatov, K.Y., and Miller, M.M., 1999, Partitioning of intermontane basins by thrust-related folding, Tien Shan, Kyrgyzstan: Basin Research, v. 11, p. 75–92, doi: 10.1046/j.1365-2117.1999.00086.x.

Busschers, F.S., Wesselingh, F.P., Kars, R.H., Versluijs-Helder, M., Wallinga, J., Bosch, J.H.A., Timmner, J., Nierop, K.G.J., Meijer, T., Bunnik, F.P.M., and De Wolf, H., 2014, Radiocarbon Dating of Late Pleistocene Marine Shells from the Southern North Sea: Radiocarbon, v. 56, p. 1151–1166, doi: 10.2458/56.16505.

Catuneanu, O., 2006, Principles of sequence stratigraphy: Elsevier.

Chappell, J., 1974, Geology of coral terraces, Huon Peninsula, New Guinea: A study of quaternary tectonic movements and sea-level changes: Bulletin of the Geological Society of America, v. 85, p. 553–570, doi: 10.1130/0016-7606(1974)85<553:GOCTHP>2.0.CO;2.

Dames and Moore, 1980, Final geoseismic investigation, proposed LNG terminal, Little Cojo Bay, California: for Western LNG Terminal Associates, 6 vols. (unpaginated).

Dibblee, T. W., 1950, Geology of southwestern Santa Barbara County California: California Department of Natural Resources Division of Mines, bulletin 150.

Dibblee, T., 1966, Geology of the Central Santa Ynez Mountains, Santa Barbara County, California: University of California, Davis.

Dibblee, T., 1978. Analysis of Geologic-Seismic Hazards to Point Conception LNG Terminal Site: Technical report to County of Santa Barbara, March1978, 72p.

Dibblee, T.W., Jr., 1988, Geologic map of the Solvang and Gaviota quadrangles, Santa Barbara Country, California: U.S. Geological Survey. Scale 1:24,000.

DOC/NOAA/NOS/OCM, 2004, 2002/2003 IfSAR data for Southern California: Digital Elevation Model (NAVD88), produced by Department of Commerce (DOC), National Oceanic and Atmospheric Administration (NOAA), National Ocean Service (NOS), Office for Coastal Management (OCM): Charleston, SC, NOAA. Accessed on 4/20/2017 at https://coast.noaa.gov/dataviewer.

DOC/NOAA/NOS/OCM, 2016 USGS West Coast El-Nino Lidar DEM (WA, OR, CA), produced by Department of Commerce (DOC), National Oceanic and Atmospheric Administration (NOAA), National Ocean Service (NOS), Office for Coastal Management (OCM): Charleston, SC, NOAA. Accessed on 7/11/2017 at https://coast.noaa.gov/dataviewer.

Duller, G., 2008, Luminescence Dating: Guidelines in Using Luminescence Dating in Archaeology: Swindon: English Heritage.

Duvall, A., Kirby, E., and Burbank, D., 2004, Tectonic and lithologic controls on bedrock channel profiles and

processes in coastal California: Journal of Geophysical Research, v. 109, p. 1–18, doi: 10.1029/2003JF000086.

Eichhubl, P., Gary Greene, H., and Maher, N., 2002, Physiography of an active transpressive margin basin: High-resolution bathymetry of the Santa Barbara basin, Southern California continental borderland: Marine Geology, v. 184, p. 95–120, doi: 10.1016/S0025-3227(01)00280-8.

Galbraith, R.F., and Roberts, R.G., 2012, Statistical aspects of equivalent dose and error calculation and display in OSL dating: An overview and some recommendations: Quaternary Geochronology, v. 11, p. 1–27, doi: 10.1016/j.quageo.2012.04.020.

Guérin, G., Mercier, N., and Adamiec, G., 2011, Dose-rate conversion factors: update: Ancient TL, v. 29, p. 5–8, http://www.aber.ac.uk/temp-ancient-tl/issue16_2/adamiec_atl_16(2)_37-50.pdf.

Gurrola, L.D., Keller, E.A., Chen, J.H., Owen, L.A., Spencer, J.Q., and Avenue, H., 2014, Tectonic geomorphology of marine terraces: Santa Barbara fold belt, California: GSA Bulletin, v. 126, p. 219–233, doi: 10.1130/B30211.1.

Holbrook, J., and Schumm, S.A., 1999, Geomorphic and sedimentary response of rivers to tectonic deformation: A brief review and critique of a tool for recognizing subtle epeirogenic deformation in modern and ancient settings: Tectonophysics, v. 305, p. 287–306, doi: 10.1016/S0040-1951(99)00011-6.

Holmquist, J.R., Reynolds, L., Brown, L.N., Southon, J.R., Simms, A.R., and MacDonald, G.M., 2015, Marine radiocarbon reservoir values in southern California estuaries: interspecies, latitudinal, and interannual variability: Radiocarbon, v. 57, p. 449–458, doi: 10.2458/azu.

Hornafius, J.S., Luyendyk, B.P., Terres, R.R., and Kamerling, M.J., 1986, Timing and extent of Neogene tectonic rotation in the western Transverse Ranges, California (USA).: Geological Society of America Bulletin, v. 97, p. 1476–1487, doi: 10.1130/0016-7606(1986)97<1476:TAEONT>2.0.CO;2.

Huntley, D., DI, G.-S., and Thewalt, M., 1985, Optical dating of sediments: Nature, v. 313, p. 105–107, doi: 10.1038/315279a0.

Ingram, B.L., and Southon, J.R., 1996, Reservoir Ages in Eastern Pacific Coastal and Estuarine Waters: Rasdiocarbon, v. 38, p. 573–582.

Jackson, J., Norris, R., and Youngson, J., 1996, The structural evolution of active fault and fold systems in central Otago, New Zealand: Evidence revealed by drainage patterns: Journal of Structural Geology, v. 18, p. 217–234, doi: 10.1016/S0191-8141(96)80046-0.

Jennings, Charles W., 1994, Fault Activity Map of California and Adjacent Areas with Location and Ages of Recent Volcanic Eruptions, California Geologic Data Map Series, Map No. 6, California Division of Mines and Geology.

Johnson, S.Y., Hartwell, S.R., Sorlien, C.C., Dartnell, P., and Ritchie, A.C., 2017, Shelf evolution along a transpressive transform margin, Santa Barbara Channel, California: Geosphere, v. 13, doi: 10.1130/GES01387.1.

Keller, E.A., and DeVecchio, D.E., 2013, Tectonic Geomorphology of Active Folding and Development of Transverse Drainages: Treatise on Geomorphology, v. 5, p. 129–147, doi: 10.1016/B978-0-12-374739-6.00088-9.

Keller, E.A., Duffy, M., Kennett, J.P., and Hill, T., 2007, Tectonic geomorphology and hydrocarbon induced topography of the Mid-Channel Anticline, Santa Barbara Basin, California: Geomorphology, v. 89, p. 274–286, doi: 10.1016/j.geomorph.2006.12.006.

Keller, E.A., Gurrola, L., and Tierney, T.E., 1999, Geomorphic criteria to determine direction of lateral propagation of reverse faulting and folding: Geology, v. 27, p. 515–518, doi: 10.1130/0091-7613(1999)027<0515:GCTDDO>2.3.CO;2.

Kennedy, G.L., Wehmiller, J.F., and Rockwell, T.K., 1992, Paleoecology and paleozoogeography of Late Pleistocene marine-terrace faunas of southwestern Santa Barbara County, California: SEPM (Society for Sedimentary Geology) Special Publication 48, p. 343-361.

Kirby, E., and Whipple, K., 2001, Quantifying differential rock-uplift rates via stream profile analysis: Geology, v. 29, p. 415–418, doi: 10.1130/0091-7613(2001)029<0415:QDRURV>2.0.CO;2.

Kirby, E., Johnson, C., Furlong, K., and Heimsath, A., 2007, Transient channel incision along Bolinas Ridge, California: Evidence for differential rock uplift adjacent to the San Andreas fault: Journal of Geophysical Research: Earth Surface, v. 112, p. 1–17, doi: 10.1029/2006JF000559.

Ku, T.L., and Kern, J.P., 1974, Uranium-series age of the upper pleistocene Nestor Terrace, San Diego, California: Bulletin of the Geological Society of America, v. 85, p. 1713–1716, doi: 10.1130/0016-7606(1974)85<1713:UAOTUP>2.0.CO;2.

47

Lajoie, K. R., Kern, J.P., Wehmiller, J.F. et al. 1979. Quaternary marine shorelines and crustal deformation, San Diego to Santa Barbara, California. *In:* ABBOT, P. L. (ed.) *Geological Excursions in the Southern California Area.* Guidebook for Field Trips, Geological Society of America Annual Meeting, November 1979. Department of Geological Sciences, San Diego State University, San Diego, CA, 3-15.

Lambeck, K., and Chappell, J., 2001, Sea Level Change Through the Last Glacial Cycle: Science, v. 292, p. 679–686, doi: 10.1126/science.1059549.

Larson, K.M., and H., W.F., 1992, Deformation in the Santa Barbara Channel from GPS Measurements 1987-1991: Geophysical Research Letters, v. 19, p. 1491–1494.

Lawson, A. C., 1893, The post-Pliocene diastrophism of the coast of southern California: University of California Publications in Geological Sciences.

Luyendyk, B.P., 1991, A model for Neogene crustal rotations, transtension, and transpression in southern California: Geological Society of America Bulletin, v. 103, p. 1528–1536, doi: 10.1130/0016-7606(1991)103<1528:AMFNCR>2.3.CO;2.

Madsen, A.T., and Murray, A.S., 2009, Optically stimulated luminescence dating of young sediments: A review: Geomorphology, v. 109, p. 3–16, doi: 10.1016/j.geomorph.2008.08.020.

Marshall, S.T., Funning, G.J., and Owen, S.E., 2013, Fault slip rates and interseismic deformation in the western Transverse Ranges, California: Journal of Geophysical Research: Solid Earth, v. 118, p. 4511–4534, doi: 10.1002/jgrb.50312.

Metcalf, J. G., 1994, Morphology, chronology, and deformation of Pleistocene marine terraces, southwestern Santa Barbara County, California, M.S. thesis, University of California, Santa Barbara.

Minor, S.A., Kellogg, K.S., Stanley, R.G., Gurrola, L.D., Keller, E.A., and Brandt, T.R., 2009, Geologic Map of the Santa Barbara Coastal Plain Area, Santa Barbara County, California: U.S. Geo logical Survey Scientific Investigations Map 3001, scale 1:25,000, 38 p., available at https://pubs.usgs.gov/sim/3001/downloads/pdf/SIM3001map.pdf

Morell, K.D., Sandiford, M., Rajendran, C.P., Rajendran, K., Alimanovic, A., Fink, D., and Sanwal, J., 2015, Geomorphology reveals active decollement geometry in the central Himalayan seismic gap: Lithosphere, v. 7, p. 247–256, doi: 10.1130/L407.1.

Muhs, D.R., Simmons, K.R., Schumann, R.R., Groves, L.T., Mitrovica, J.X., and Laurel, D., 2012, Sea-level history during the Last Interglacial complex on San Nicolas Island, California: Implications for glacial isostatic adjustment processes, paleozoogeography and tectonics: Quaternary Science Reviews, v. 37, p. 121–133, doi: 10.1016/j.quascirev.2012.01.010.

Murray, A.S., and Wintle, A.G., 2000, Luminescence dating of quartz using an improved single- aliquot regenerative-dose protocol: Radiation Measurements, v. 32, p. 57–73, doi: 10.1016/S1350-4487(99)00253-X.

Nelson, Zachary, 2018, Late Pleistocene to Holocene environmental history of Devereux Slough, M.S. thesis, University of California, Santa Barbara.

Ouchi, S., 1985, Response of alluvial rivers to slow active tectonic movement: Geological Society of America Bulletin, v. 96, p. 504–515, doi: 10.1130/0016-7606(1985)96<504:ROARTS>2.0.CO;2.

Price, G.J., Webb, G.E., Zhao, J. xin, Feng, Y. xing, Murray, A.S., Cooke, B.N., Hocknull, S.A., and Sobbe, I.H., 2011, Dating megafaunal extinction on the Pleistocene Darling Downs, eastern Australia: The promise and pitfalls of dating as a test of extinction hypotheses: Quaternary Science Reviews, v. 30, p. 899–914, doi: 10.1016/j.quascirev.2011.01.011.

Redin, T., Forman, J., Kamerling, M., and Galloway, J., 2005, Santa Barbara Channel structure and correlation sections—CS32 to CS-42: American Association of Petroleum Geologists, Pacific Section, Publication CS 36, 12 sheets.

Reimer, P., Bard, E., Bayliss, A., Beck, J., Blackwell, P., Ramsey, C., Buck, C., Cheng, H., Edwards, R., Friedrich, M., Grootes, P., Guilderson, T., Haflidason, H., Hajdas, I., et al., 2013, IntCal13 and Marine13 radiocarbon age calibration curves 0 – 50,000 years cal BP: Radiocarbon, v. 55, p. 1869–1887, doi: 10.2458/rc.v51i4.3569.

Reynolds, L.C., 2018, The late Quaternary evolution of the southern California coast: sea-level change, storms, and subsidence, doctoral dissertation, University of California, Santa Barbara.

Rhodes, E.J., 2011, Optically Stimulated Luminescence Dating of Sediments over the Past 200,000 Years: Annual Review of Earth and Planetary Sciences, v. 39, p. 461–488, doi: 10.1146/annurev-earth-040610-133425.

Rittenour, T.M., 2008, Luminescence dating of fluvial deposits: Applications to geomorphic, palaeoseismic and archaeological research: Boreas, v. 37, p. 613–635, doi: 10.1111/j.1502-3885.2008.00056.x.

Rockwell, T.K., Nolan, J., Johnson, D.L., and Patterson, R.H., 1992, Ages and Deformation of Marine Terraces Between Point Conception and Gaviota, Western Transverse Ranges, California: SEPM (Society for Sedimentary Geology).

Rockwell, T.K., Clark, K., Gamble, L., Oskin, M.E., Haaker, E.C., and Kennedy, G.L., 2016, Large Transverse Range Earthquakes Cause Coastal Upheaval near Ventura, Southern California: Bulletin of the Seismological Society of America, v. 106, p. 2706–2720, doi: 10.1785/0120150378.

SCEC, 1995, Seismic hazards in southern California: Probable earthquakes, 1994 to 2024: Bulletin of the Seismological Society of America, v. 85, p. 379-439.

Schwanghart, W., and Scherler, D., 2014, Short Communication: TopoToolbox 2 - MATLAB-based software for topographic analysis and modeling in Earth surface sciences: Earth Surface Dynamics, v. 2, p. 1–7.

Schwarcz, H.P., 2002, Chronometric dating in archaeology: A review: Accounts of Chemical Research, v. 35, p. 637–643, doi: 10.1021/ar010039o.

Shackleton, N.J., 1987, Oxygen isotopes, ice volume and sea level: Quaternary Science Reviews, v. 6, p. 183–190, doi: 10.1016/0277-3791(87)90003-5.

Simms, A.R., Rouby, H., and Lambeck, K., 2016, Marine terraces and rates of vertical tectonic motion: The importance of glacio-isostatic adjustment along the Pacific coast of central North America: Bulletin of the Geological Society of America, v. 128, p. 81–93, doi: 10.1130/B31299.1.

Sorlien, C.C., and Nicholson, C., 2015, Post-1 Ma Deformation History of the Pitas Point-North Channel-Red Mountain Fault System and Associated Folds in Santa Barbara Channel, California.:

Southern California Earthquake Data Center, 2018, Southern California Earthquake Catalog: Southern California Earthquake Data Center database, accessed May 21, 2018, available at http://www.data.scec.org/eq-catalogs/index.html.

Stuiver, M., and Reimer, P.J., 1993, Radiocarbon: v. 35, p. 215–230.

Stuiver, M., Reimer, P.J., and Reimer, R.W., 2017, CALIB 7.1 [www program] at http://calib.org, accessed 2017-9-11.

Sylvester, A.G., 2001, Catalog of Santa Barbara Earthquakes—1800 to 1960: University of California, Santa Barbara, accessed July 3, 2018, available at https://projects.eri.ucsb.edu/sb_eqs/SBEQCatlog/SBEQCATINTRO.html.

Sylvester, A.G., and Darrow, A.C., 1979, Structure and neotectonics of the western Santa Ynez fault system in southern California: Tectonophysics, v. 52, p. 389–405.

Sylvester, A.G., Smith, Stewart, W., and Scholz, C.H., 1970, Earthquake swarm in the Santa Barbara Channel, California, 1968: Bulletin of the Seismological Society of America, v. 60, doi: 10.1785/0120160029.

Tierney, T.E., 2002. Tectonic geomorphology of the greater Santa Ynez Mountains, Santa Barbara County, California. M.S. thesis, University of California, Santa Barbara.

Trecker, M.A., Gurrola, L.D., and Keller, E.A., 1998, Oxygen-isotope correlation of marine terraces and uplift of the Mesa Hills, Santa Barbara, California, USA: Geological Society, London, Special Publications, v. 146, p. 57–69.

Upson, J.E., 1951, Former marine shore lines of the Gaviota Quadrangle, Santa Barbara County, California: Journal of Geology, v. 59, p. 415–446.

Wampler, D.F., 2013, Tectonic Geomorphology of the Gaviota Coast, M.S. thesis, University of California, Santa Barbara.

Weil, J.A., 1984, A review of electron spin spectroscopy and its application to the study of paramagnetic defects in crystalline quartz: Physics and Chemistry of Minerals, v. 10, p. 149–165, doi: 10.1007/BF00311472.

Wells, D.L., and Coppersmith, K.J., 1994, New Empirical Relationships among Magnitude, Rupture Length, Rupture Width, Rupture Area, and Surface Displacement: Bulletin of the Seismological Society of America, v. 84, p. 974–1002.

Wobus, C., Whipple, K.X., Kirby, E., Snyder, N., Johnson, J., Spyropolou, K., Crosby, B., and Sheehan, D., 2006, Tectonics from topography: procedurses, promise, and pitfalls: Geological Society of America Special Paper, v. 398, p. 55–74, doi: 10.1130/2006.2398(04).

Yerkes, R.F., Greene, H.G., Tinsley, J.C., and Lajoie, K.R., 1981, Maps showing seismotectonic setting of the Santa Barbara channel area, California, U.S. Geological Survey, Misc. field studies map, No. 1169, 25p., Scale 1:250,000.

Youngs, R.R., and Coppersmith, K.J., 1985, Implications of fault slip rates and earthquake recurrence models to probabilisic seismic hazard estimates: Bulletin of the Seismological Society of America, v. 75, p. 939–964.

APPENDIX

Optically stimulated luminescence lab procedures

In the OSL lab, sediment was removed from sampling tubes under low-level orange light. Potentially light-exposed material from the outer ends of tubes was removed and discarded prior to processing. The remaining sediment from the center of sample tubes was wet sieved to 125-212 μm or 150-250 μm grain size fractions, depending on the sample grain size. Sieved fractions were then treated with HCl and H_2O_2 to remove carbonates and reactive organic material, respectively. The remaining material was subsequently etched with hydrofluoric acid to remove potentially alpha-irradiated surface layers from sand grains. Finally, samples were rinsed in HCl again to remove any fluoride byproducts. Quartz grains were then isolated from K-spar or other minerals via heavy mineral separation. Finally, sample luminescence was measured with a Risø TL/OSL Model DA-20 reader following the single-aliquot regenerative-dose (SAR) protocol (Murray and Wintle, 2000), with blue-green light stimulation.
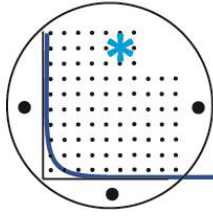
Project: **Gaviota Coast Terraces**   Project #: **279**
Scientist: **Daniel Morel, Univ. of CA, Santa Barbara**
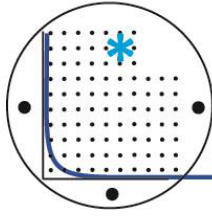Report by: **Tammy Rittenour**   Report date: **May 25, 2018**

Equivalent dose (D_E) Distributions: Probability density functions and radial plots

1. ENP_OSL_01, USU-2595
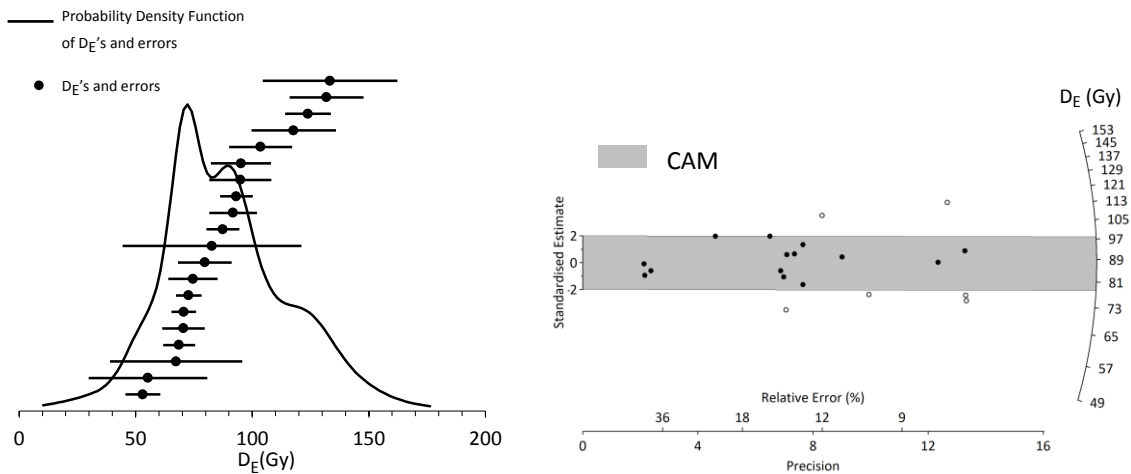
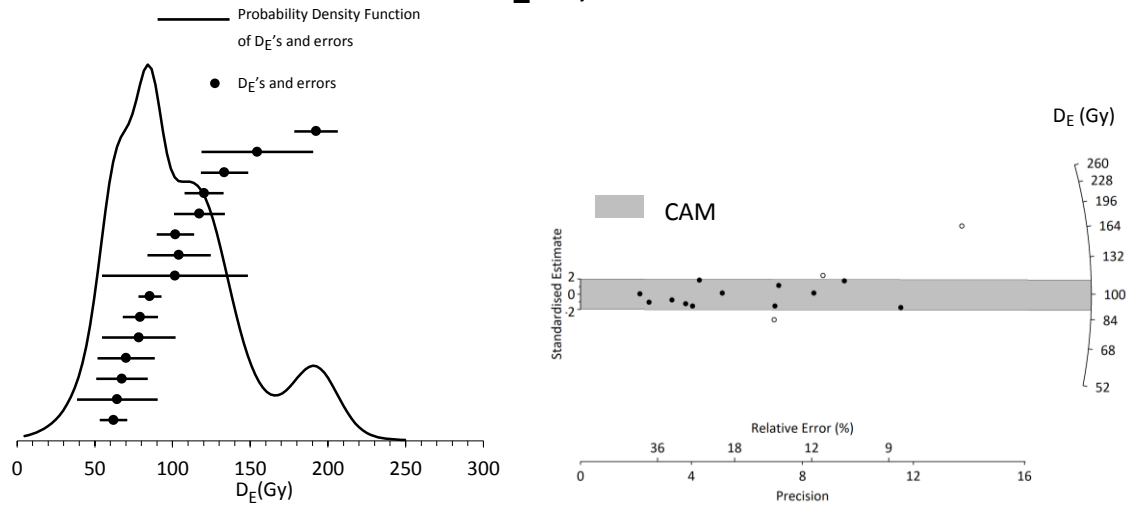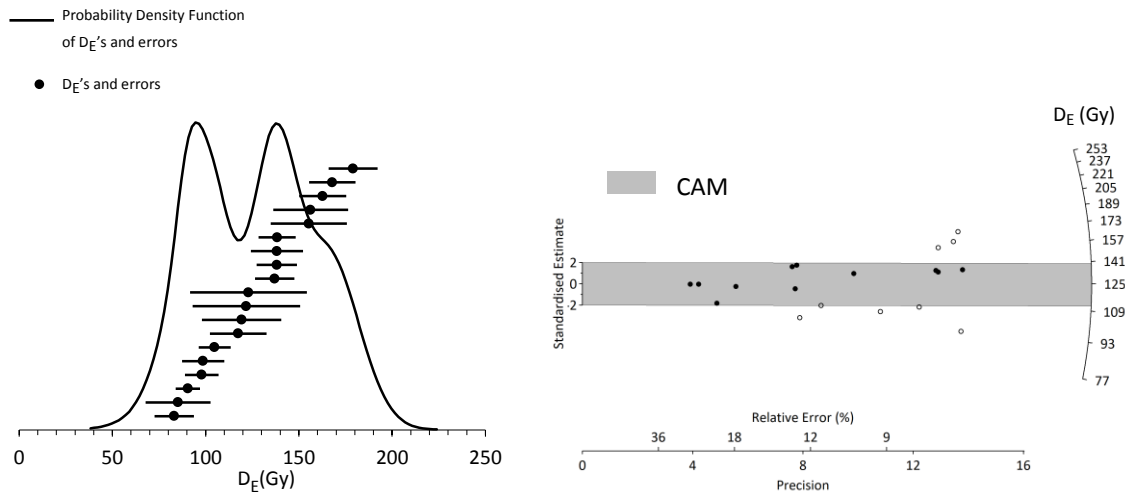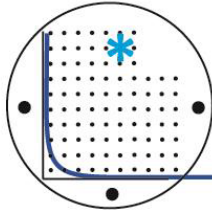### 2. ENP_OSL_02, USU-2596

51

USU LUMINESCENCE LABORATORY
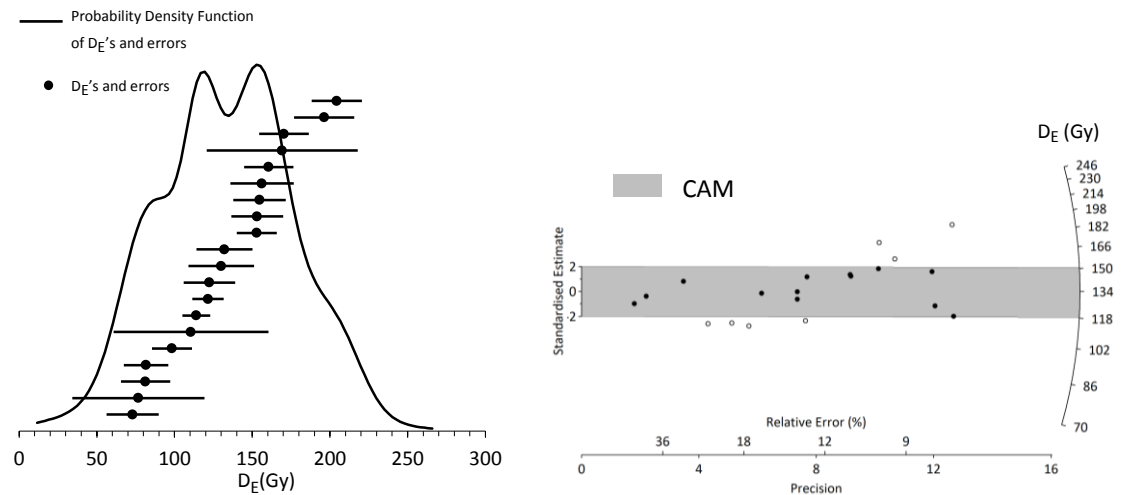
Equivalent dose (D$_E$) Distributions: Probability density functions and radial plots
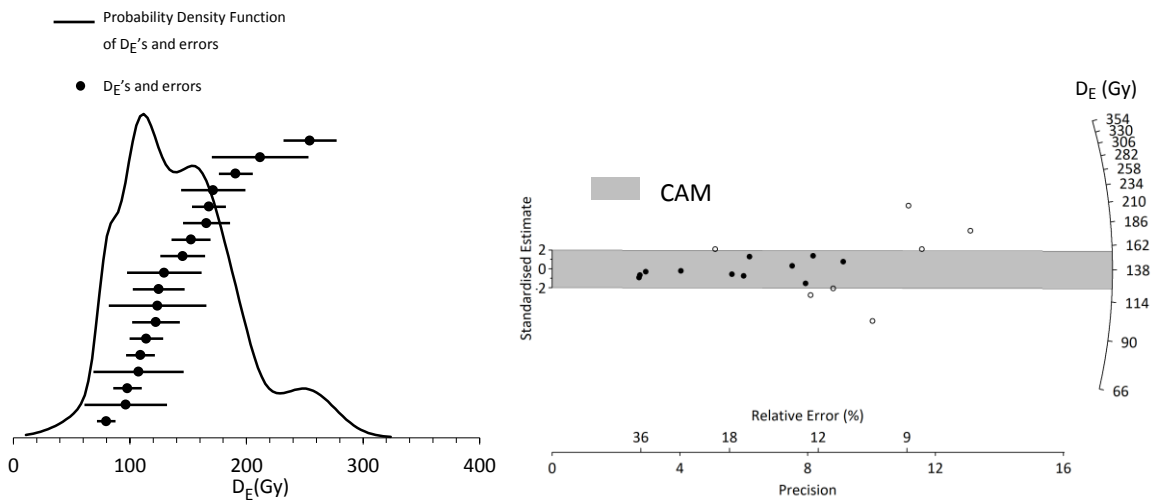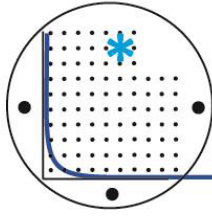
3. WNP_OSL, USU-2597

4. WLV_OSL, USU-2598

Equivalent dose (D$_E$) Distributions: Probability density functions and radial plots
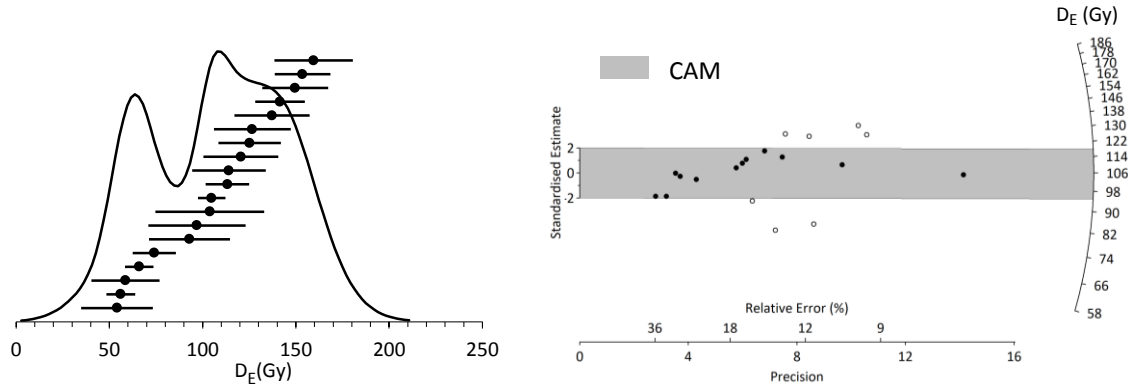
5. WEC_OSL, USU-2599
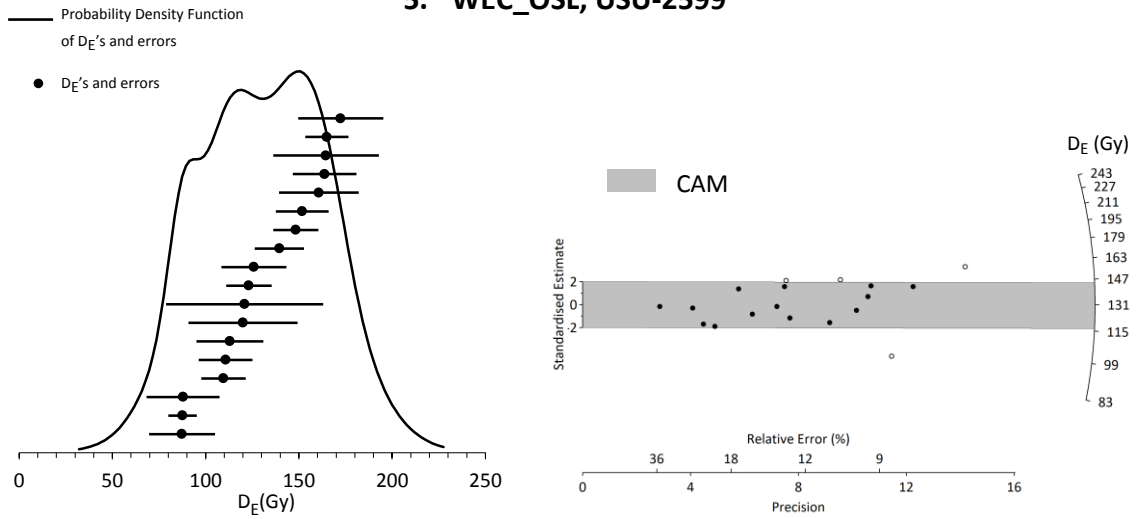
6. EAC_OSL, USU-2660

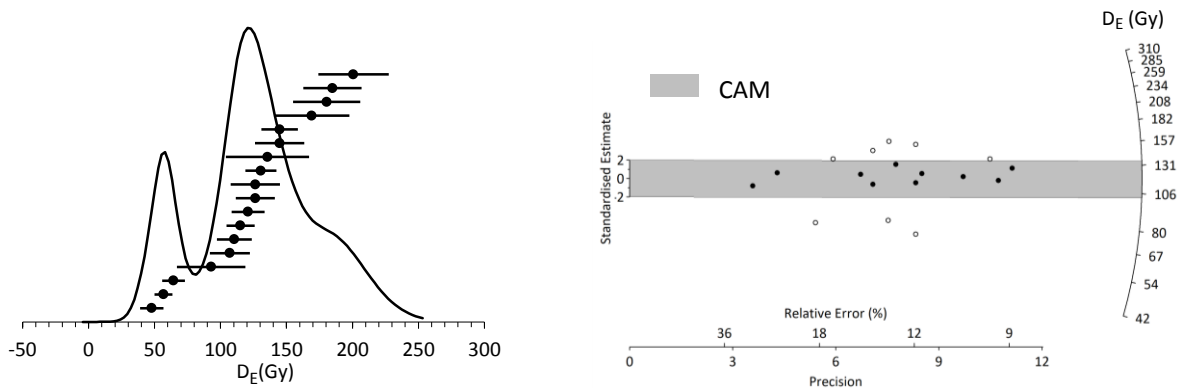### Equivalent dose (D$_E$) Distributions: Probability density functions and radial plots
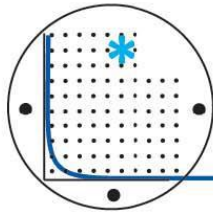
7. WSAG_OSL_01, USU-2661

——— Probability Density Function
of D$_E$'s and errors

● D$_E$'s and errors

8. WSAG_OSL_02, USU-2662

——— Probability Density Function
of D$_E$'s and errors

● D$_E$'s and errors

Procedures for sample processing and small-aliquot OSL age analysis:

All samples were opened and processed under dim amber safelight conditions within the lab. Sample processing for quartz optically stimulated luminescence (OSL) dating followed standard procedures involving sieving, HCl and bleach treatments, heavy mineral separation at 2.72 g/cm$_3$, and acid treatments with HCl and HF to isolate the quartz component of a narrow grain-size range (150- 250 µm and 125-212 µm). The purity of the quartz samples was checked by measurement with infra-red stimulation to detect the presence of feldspar.

The USU Luminescence Lab follows the latest single-aliquot regenerative-dose (SAR) procedures for OSL dating of quartz sand (Murray and Wintle, 2000, 2003; Wintle and Murray, 2006). The SAR protocol includes tests for sensitivity correction and brackets the equivalent dose (D$_E$) the sample received during burial by irradiating the sample at five different doses (below, at, and above the D$_E$, plus a zero dose and a repeated dose to check for recuperation of the signal and sensitivity correction). The resultant data are fit with a saturating exponential curve from which the D$_E$ is calculated on the Central Age Model (CAM) of Galbraith and Roberts (2012). The OSL age is reported at 2σ standard error and is calculated by dividing the D$_E$ (in grays, gy) by the environmental dose rate (gy/ka) that the sample has been exposed to during burial.

Dose-rate calculations were determined by chemical analysis of the U, Th, K and Rb content using ICP-MS and ICP-AES techniques and conversion factors from Guérin et al. (2011). The contribution of cosmic radiation to the dose rate was calculated using sample depth, elevation, and latitude/longitude following Prescott and Hutton (1994). Dose rates are calculated based on water content, sediment chemistry, and cosmic contribution (Aitken and Xie, 1990; Aitken, 1998).

Under the collaborative agreement to analyze samples at the USU Luminescence Lab, please consider including Dr. Rittenour as a co-author on resultant publications. Contact me for additional information and help with describing the OSL technique when you plan your publication.
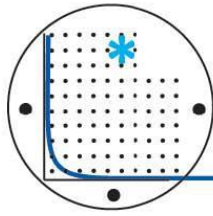
Dr. Tammy Rittenour

Director   Associate Professor
USU Luminescence Lab   Dept. of Geology, Utah State University
1770 N Research parkway, suite 123   4505 Old Main Hill
North Logan, UT 84341   Logan, UT 84322-4505

tammy.rittenour@usu.edu   http://www.usu.edu/geo/luminlab/

USU LUMINESCENCE LABORATORY
http://usu.edu/geo/luminlab
1770 North Research Parkway, Suite 123, North Logan, Utah 84341

References cited:

Aitken, M.J. 1998: An Introduction to Optical Dating: The dating of Quaternary sediments by the use of photon-stimulated luminescence. New York, Oxford University Press, 267 p.

Aitken, M.J., Xie, J., 1990. Moisture correction for annual gamma dose. Ancient TL 8 (2), 6-9.

Galbraith, R.F., Roberts, R.G., 2012. Statistical aspects of equivalent dose and error calculation and display in OSL dating: An Overview and some recommendations. Quaternary Geochronology 11, 1-27.

Guérin, G., Mercier, N., Adamiec, G., 2011. Dose-rate conversion factors: update: Ancient TL 29, 5-8.

Murray, A.S., Wintle, A.G., 2000. Luminescence dating of quartz using an improved single aliquot regenerative-dose protocol. Radiation Measurements 32, 57-73.

Murray, A.S., Wintle, A.G., 2003. The single aliquot regenerative dose protocol: potential for improvements in reliability. Radiation Measurements 37, 377-381.

Prescott, J. R., Hutton, J.T., 1994. Cosmic ray contributions to dose rates for luminescence and ESR dating: Radiation Measurements 23, 497-500.

Wintle, A.G. Murray, A.S., 2006. A review of quartz optically stimulated luminescence characteristics and their relevance in single-aliquot regenerative protocols: Radiation Measurements, v. 41, p. 369-391.